Spectroscopic Studies of the Coupled Binuclear Non-Heme Iron Active Site in the Fully Reduced Hydroxylase Component of Methane Monooxygenase: Comparison to Deoxy and Deoxy-Azide Hemerythrin

Sabine Pulver,[†] Wayne A. Froland,[‡] Brian G. Fox,[‡,§] John D. Lipscomb,*[,‡] and Edward I. Solomon*[,†]

Contribution from the Department of Chemistry, Stanford University, Stanford, California 94305, and Department of Biochemistry, University of Minnesota, Minneapolis, Minnesota 55455

Received June 28, 1993[⊗]

Abstract: A combination of circular dichroism (CD) and magnetic circular dichroism (MCD) spectroscopies has been used to probe the geometric and electronic structure of the binuclear Fe(II) active site of the reduced hydroxylase component of methane monooxygenase (MMOH). Excited-state data provide the numbers and energies of d → d transitions which are interpreted in terms of ligand field calculations to estimate the geometry of each iron. Variable-temperature variable-field (VTVH) MCD data are analyzed by using a non-Kramers doublet model to obtain the zero field splitting (ZFS) and $g_{\|}$ value of the ground state and the excited sublevel energies. These results are further interpreted in terms of a spin Hamiltonian which includes the ZFS of each Fe^{2+} combined with the exchange coupling between iron centers. The reduced MMOH contains two five-coordinate ferrous centers with different geometries. VTVH MCD data show the ferrous centers to be ferromagnetically coupled with $J \sim 0.3$–0.5 cm^{-1} for the reduced hydroxylase. This indicates that in contrast to deoxyHr which has a binuclear Fe^{2+} site that is antiferromagnetically coupled through a hydroxide bridge, fully reduced MMOH may have a water bridge. The addition of anions, substrates, and inhibitors to reduced MMOH results in no change in the CD spectrum suggesting that these molecules do not bind to the iron or cause large perturbations in the iron site. In contrast, addition of component B causes dramatic changes in the CD and MCD spectra which indicate that one iron in the biferrous active site is altered. Two ferromagnetically coupled Fe(II) centers with distorted five-coordinate square-pyramidal geometries are also found for the MMOH-component B complex. Geometric and electronic structural changes resulting from the addition of component B to reduced MMOH are described and correlated with enhanced reactivity. The above results are compared to parallel results for deoxyHr, and differences are correlated to the difference in dioxygen reactivity (binding versus activation).

Introduction

A coupled binuclear non-heme iron active site exists in a variety of different enzymes and proteins whose function often involves reaction with dioxygen.[1-5] The term "coupled" refers to the fact that the sites show magnetic coupling between the iron atoms which is associated with the presence of a bridging ligand. Members of this class of proteins include hemerythrin (Hr),[6,7] methane monooxygenase (MMO),[8-11] ribonucleotide diphosphate reductase (RDPR),[12-15] the purple acid phosphatases (PAP)[16,17] including uteroferrin (Uf),[18,19] ruberythrin (Rb),[20] and stearoyl acyl carrier protein Δ^9 desaturase.[21] The binuclear iron site can exist in three oxidation states: met or oxidized [Fe(III)Fe(III)], half-met or mixed-valent [Fe(II)Fe(III)], and deoxy or fully reduced [Fe(II)Fe(II)]. All three oxidation states can be obtained in Hr and MMOH.

Hemerythrin is an oxygen transport protein in which dioxygen reacts with the binuclear ferrous state to form the oxyHr site which has peroxide bound to one ferric ion in an end on fashion.[1,3,5] Spectroscopic studies on the met forms of Hr have shown that both Fe^{3+} ions are high-spin with a large antiferromagnetic exchange coupling (for metHr $J = -134$ cm^{-1} using $\mathcal{H} = -2JS_1 \cdot S_2$)[22] mediated by an oxo bridge.[23-27] The 2.0 Å crystal

† Stanford University.
‡ University of Minnesota.
§ Present address: Department of Biochemistry, Institute for Enzyme Research, University of Wisconsin, Madison, WI 53705.
⊗ Abstract published in *Advance ACS Abstracts*, December 1, 1993.

(1) Vincent, J. B.; Olivier-Lilley, G. L.; Averill, B. A. *Chem. Rev.* **1990**, *90*, 1447–1467.
(2) Sanders-Loehr, J. In *Iron Carriers and Iron Proteins*; T. M. Loehr, Ed.; VCH Press: New York, 1989; pp 373–466.
(3) Que, L.; True, A. E. In *Progress in Inorganic Chemistry: Bioinorganic Chemistry*; Lippard, S. J., Ed.; John Wiley & Sons: New York, 1990; Vol. 38, pp 97–200.
(4) Kurtz, D. M. *Chem. Rev.* **1990**, *90*, 585–606.
(5) Howard, J. B.; Rees, D. C. In *Advances in Protein Chemistry*; Anfinsen, C. B., Edsall, J. T., Eisenberg, D. S., Richards, F. M., Eds.; Academic Press Inc.: San Diego, 1991; Vol. 42, pp 199–280.
(6) Wilkins, P. C.; Wilkins, R. G. *Coord. Chem. Rev.* **1987**, *79*, 195–214.
(7) Klotz, I. M.; Kurtz, D. M. *Acc. Chem. Res.* **1984**, *17*, 16–22.
(8) Fox, B. G.; Froland, W. A.; Dege, J. E.; Lipscomb, J. D. *J. Biol. Chem.* **1989**, *264*, 10023–10033.
(9) Froland, W. A.; Andersson, K. K.; Lee, S.-K.; Liu, Y.; Lipscomb, J. D. In *Microbial Growth on C_1 Compounds*; Murrell, J. C., Kelly, D. P., Eds.; Intercept Ltd.: Andover, 1993; pp 81–92.
(10) Fox, B. G.; Lipscomb, J. D. In *Biological Oxidation Systems*; Reddy, C. C., Hamilton, G. A., Madyastha, K. M., Eds.; Academic Press: New York, 1992; Vol. 1, pp 367–388.
(11) Dalton, H. In *Advances in Applied Microbiology*; Umbreit, W. W., Ed.; Academic Press: New York, 1980; Vol. 26, pp 71–87.
(12) Stubbe, J. *J. Biol. Chem.* **1990**, *265*, 5329–5332.
(13) Bollinger, J. M.; Edmondson, D. E.; Huynh, B. H.; Filley, J.; Norton, J. R.; Stubbe, J. *Science* **1991**, *253*, 292–298.
(14) Nordlund, P.; Sjöberg, B.-M.; Eklund, H. *Nature* **1990**, *345*, 593–598.
(15) Reichard, P.; Ehrenberg, A. *Science* **1983**, *221*, 514–519.
(16) Doi, K.; Antanaitis, C.; Aisen, P. In *Structure and Bonding*; Clarke, M. J., Goodenough, J. B., Ibers, J. A., Jorgensen, C. K., Mingos, D. M. P., Neilands, J. B., Palmer, G. A., Reinen, D., Sadler, P. J., Weiss, R., Williams, R. J. P., Eds.; Springer-Verlag: Heidelberg, 1988; Vol. 70, pp 1–26.
(17) Vincent, J. B.; Averill, B. A. *FASEB J.* **1990**, *4*, 3009–3014.
(18) Antanaitis, B. C.; Aisen, P. In *Frontiers in Bioinorganic Chemistry*; Xavier, A. V., Ed.; VCH: New York, 1986; pp 481–493.
(19) Que, L.; Scarrow, R. C. In *Metal Clusters in Proteins*; Que, L., Ed.; American Chemical Society: Washington, DC, 1988; pp 152–178.
(20) LeGall, J.; Prickril, B. C.; Moura, I.; Xavier, A. V.; Moura, J. J. G.; Huynh, B.-H. *Biochemistry* **1988**, *27*, 1636–1642.
(21) Fox, B. G.; Shanklin, J.; Somerville, C.; Münck, E. *Proc. Natl. Acad. Sci. U.S.A.* **1993**, *90*, 2486–2490.
(22) Schugar, H. J.; Rossman, G. R.; Barraclough, C. G.; Gray, H. B. *J. Am. Chem. Soc.* **1972**, *94*, 2683–2690.

0002-7863/93/1515-12409$04.00/0

structure of metHr confirmed the presence of the oxo bridge as well as two carboxylate bridges.[28,29] The crystal structure also showed that one Fe^{3+} is six-coordinate with three histidine ligands in addition to the carboxylate bridges, and the other is five-coordinate with only two histidine ligands.

DeoxyHr has been studied with a combination of near-infrared absorption (NIR ABS), CD and MCD spectroscopies which have shown that the deoxyHr site consists of one five- and one six-coordinate Fe(II), and has significantly lower antiferromagnetic exchange coupling ($-12 \leq -J \leq -38$ cm^{-1}) than metHr.[30,31] The relatively low magnitude of the antiferromagnetic coupling constant indicates that the oxo group bridging the ferric ions in metHr becomes protonated upon reduction resulting in a binuclear ferrous site bridged by hydroxide.[30] X-ray crystallographic studies subsequently confirmed the coordination geometries of the iron atoms in the deoxyHr active site.[32] Small molecule binding studies with azide, cyanate, and fluoride demonstrated that these ligands bind to the open coordination position on the five-coordinate Fe(II) of deoxyHr resulting in two six-coordinate Fe(II) ions.[30] These deoxy derivatives show significant MCD intensity at lowest temperature indicating that all three have a paramagnetic non-Kramers ground state. Variable-temperature variable-field (VTVH) MCD studies on deoxyHrN_3^- demonstrated that the ground state has a $g_{eff} = 16.7$ which requires that the two ferrous ions be ferromagnetically coupled with each undergoing zero field splitting (negative) to produce an $S_{Tot} = 4$, $M_S = \pm 4$ ground state. Based on the constrained nature of the Hr active site and the fact that both Fe(II) ions are six-coordinate in deoxyN_3^-Hr, it was suggested that the change in the magnetic behavior with respect to deoxyHr is the result of protonation of the bridging OH^- present in deoxyHr to form a H_2O bridge in deoxyN_3^-Hr.[30]

Methane monooxygenase catalyzes the conversion of methane to methanol in methanotrophic bacteria by way of the following reaction:[11]

$$CH_4 + NADH + H^+ + O_2 \rightarrow CH_3OH + NAD^+ + H_2O$$

The soluble form of methane monoxygenase (EC 1.14.13.25) isolated from *Methylosinus trichosporium* OB3b is a three-component enzyme consisting of a 245-kDa hydroxylase (MMOH) with an $(\alpha, \beta, \gamma)_2$ subunit structure, a 40-kDa reductase, and a 15.8-kD monomeric protein known as component B (MMOB).[8] The reductase contains one FAD and one [2Fe-2S] cluster[33,34] and participates in the transfer of reducing equivalents from NADH to the hydroxylase.[8,35] Component B contains no metals or cofactors[36] and plays an unknown regulatory role in catalysis, although it is not required for enzyme turnover.[8,37] The hydroxylase consists of two non-heme iron clusters each containing a coupled binuclear iron active site.[8,33,38,39] This active site is responsible for methane conversion.[8,40]

Mössbauer and electron paramagnetic resonance (EPR) studies on the oxidized hydroxylase demonstrate that the biferric center is diamagnetic at low temperature due to antiferromagnetic coupling between the two $S = {}^5/_2$ iron atoms.[33,38,41] Extended X-ray absorption fine structure (EXAFS) studies on this form give an Fe–Fe distance of 3.4 Å and indicate that a short μ-oxo bridge does not appear to be present in MMOH.[39] This is in contrast to metHr and is reflected in a reduced exchange coupling in met MMOH.[33] The mixed-valent half-met state of MMOH is EPR active.[8] It exhibits a rhombic EPR spectrum with g values all less than 2 ($g_{av} = 1.85$),[8] resembling the EPR spectra of half-met Hr.[42,43] Upon full reduction of the hydroxylase the high-spin ferrous ions ($S = 2$) become ferromagnetically coupled ($S_{Tot} = 4$) to give an integer spin EPR signal near $g_{eff} = 16$[38,44] similar to that observed in deoxyazide Hr.[30]

In this paper, we use a combination of excited-state spectral methods (CD and low-temperature MCD) to study the ligand field region from 5000 to 20 000 cm^{-1} and VTVH MCD to probe the ground-state sublevels of MMOH. The focus of this study is the application of the excited-state protocol developed for deoxy and deoxyN_3^-Hr[30] to reduced MMOH. In addition, the interaction of the fully reduced MMOH active site with substrates, inhibitor, small molecules, and component B has been investigated. This study allows the definition of differences and similarities in the electronic and geometric structure of deoxyHr, deoxyN_3^-Hr, and reduced MMOH, the results of which are related to differences in the reactivity of these proteins with molecular oxygen (O_2 activation in MMOH as compared to reversible O_2 binding in Hr).

Experimental Section

All commercial reagents were used as obtained: D_2O 99.9 atom % D; Aldrich), glycer(ol-d_3) (98 atom % D; Aldrich), MOPS buffer (Sigma), sodium hydrosulfite (Fisher), methyl viologen (Sigma), sodium azide (Aldrich), sodium chloride (Mallinckrodt), potassium cyanate (Mallinckrodt), potassium thiocyanide (Fisher), sodium cyanide (Baker), sodium fluoride (Mallinckrodt), imidazole (Aldrich), dimethyl sulfoxide (Aldrich), methanol (Baker), acetonitrile (Aldrich), *trans*-1,2-dichloroethylene (Aldrich), and tetrachloroethylene (Baker).

Soluble MMO from *Methylosinus trichosporium* OB3b was purified and characterized as described previously.[8,45] The specific activity of the hydroxylase was 1000–1200 nmol/min/mg (4 mol Fe/mol hydroxylase), while that of the component B was 10 000 nmol/min/mg. For NIR CD studies all MMOH and MMOB used was exchanged into 200 mM NaMOPS, 5% (^{1}H)-glycerol, pD = 7.4 (99.9% D_2O) (buffer A) by use of a Sephadex G-25 desalting column (1.4 cm × 5.0 cm) equilibrated with buffer A. Typically, concentrated protein was diluted with buffer A and passed through the desalting column. The deuterated MMOH was then reconcentrated to 250–300 mg/mL by use of both an Amicon ultrafiltration cell fit with a YM-100 membrane and Centricon-100 microconcentrators. The same procedure was followed with MMOB except that a YM-5 membrane was used with the ultrafiltration and Centricon-3 microconcentrators were utilized.

Fully reduced samples of MMOH were prepared by placing the oxidized hydroxylase in a conical reaction vial with 100 μM methyl viologen, all in 400 mM MOPS buffer, pD 7.6. The samples were made anaerobic by repeated cycles of evacuation and flushing with O_2-scrubbed nitrogen and subsequently reduced by addition of an excess of sodium dithionite

(23) Hendrickson, W. A.; Co, M. S.; Smith, J. L.; Hodgson, K. O.; Klippenstein, G. L. *Proc. Natl. Acad. Sci. U.S.A.* **1982**, *79*, 6255–6259.
(24) Elam, W. T.; Stern, E. A.; McCallum, J. D.; Sanders-Loehr, J. *J. Am. Chem. Soc.* **1983**, *105*, 1919–1923.
(25) Shiemke, A. K.; Loehr, T. M.; Sanders-Loehr, J. *J. Am. Chem. Soc.* **1984**, *106*, 4951–4956.
(26) Freier, S. M.; Duff, L. L.; Shriver, D. F.; Klotz, I. M. *Arch. Biochem. Biophys.* **1980**, *205*, 449–463.
(27) Gay, R. R.; Solomon, E. I. *J. Am. Chem. Soc.* **1978**, *100*, 1972–1973.
(28) Stenkamp, R. E.; Sieker, L. C.; Jensen, L. H. *J. Am. Chem. Soc.* **1984**, *106*, 618–622.
(29) Holmes, M. A.; Stenkamp, R. E. *J. Mol. Biol.* **1991**, *220*, 723–737.
(30) Reem, R. C.; Solomon, E. I. *J. Am. Chem. Soc.* **1987**, *109*, 1216–1226.
(31) Solomon, E. I.; Zhang, Y. *Acc. Chem. Res.* **1992**, *25*, 343–352.
(32) Holmes, M. A.; Trong, I. L.; Turley, S.; Sieker, L. C.; Stenkamp, R. E. *J. Mol. Biol.* **1991**, *218*, 583–593.
(33) Fox, B. G.; Hendrich, M. P.; Surerus, K. K.; Andersson, K. K.; Froland, W. A.; Lipscomb, J. D.; Münck, E. *J. Am. Chem. Soc.* **1993**, *115*, 3688–3701.
(34) Green, J.; Dalton, H. *J. Biol. Chem.* **1985**, *260*, 15 795–15 801.
(35) Prince, R. C.; Patel, R. N. *FEBS Lett.* **1988**, *203*, 127–130.
(36) Lund, J.; Dalton, H. *Eur. J. Biochem.* **1985**, *147*, 291–296.
(37) Froland, W. A.; Andersson, K. K.; Lee, S.-K.; Liu, Y.; Lipscomb, J. D. *J. Biol. Chem.* **1992**, *267*, 17 588–17 597.
(38) Fox, B. G.; Surerus, K. K.; Münck, E.; Lipscomb, J. D. *J. Biol. Chem.* **1988**, *263*, 10 553–10 556.
(39) DeWitt, J. G.; Bentsen, J. G.; Rosenzweig, A. C.; Hedman, B.; Green, J.; Pilkington, S.; Papaefthymiou, G. C.; Dalton, H.; Hodgson, K. O.; Lippard, S. J. *J. Am. Chem. Soc.* **1991**, *113*, 9219–9235.
(40) Andersson, K. K.; Froland, W. A.; Lee, S.-K.; Lipscomb, J. D. *New J. Chem.* **1991**, *15*, 411–415.
(41) Fox, B. G.; Lipscomb, J. D. *Biochem. Biophys. Res. Commun.* **1988**, *154*, 165–170.
(42) McCormick, J. M.; Reem, R. C.; Solomon, E. I. *J. Am. Chem. Soc.* **1991**, *113*, 9066–9079.
(43) Muhoberac, B. B.; Wharton, D. C.; Babcock, L. M.; Harrington, P. C.; Wilkins, R. G. *Biochim. Biophys. Acta* **1980**, *626*, 337–345.
(44) Hendrich, M. P.; Münck, E.; Fox, B. G.; Lipscomb, J. D. *J. Am. Chem. Soc.* **1990**, *112*, 5861–5865.
(45) Fox, B. G.; Froland, W. A.; Jollie, D. R.; Lipscomb, J. D. *Methods Enzymol.* **1990**, *188*, 191–202.

(six reducing equivalents based on the presence of two binuclear iron clusters per hydroxylase molecule). The protein was allowed to incubate for approximately 15 min at room temperature and then transferred to an appropriate sample holder.

The effects of small molecule binding were investigated by the anaerobic addition of microliter quantities of a thoroughly degassed ligand solution to the fully reduced MMOH in a CD cell. All ligand solutions were prepared in D_2O unless otherwise noted. The concentration of small molecules added to the protein sample was varied, up to a 400-fold molar excess. Samples probing enzyme–substrate interactions were studied by the addition of microliter quantities of an anaerobic stock solution (15–25 mM for *trans*-1,2-dichloroethylene; 5 mM for tetrachloroethylene) to the reduced hydroxylase in the CD cell. Typically a 2–3-fold molar excess of substrate was used in the CD experiments. The solubility of *trans*-1,2-dichloroethylene ($C_2H_2Cl_2$) was determined at 23 °C in 0.2 M MOPS buffer, pD 7.6, under anaerobic conditions through NMR proton integration using tetrahydrofuran as the reference. The solubility of tetrachloroethylene was obtained from previously published data.[46] Samples of the anaerobic hydroxylase-component B complex were prepared by the addition of a 2–4-fold molar excess of anaerobic component B to reduced MMOH in the CD cell or reaction vial. All samples were incubated for approximately 15 min before spectra were taken.

Room temperature NIR CD spectra (600–2000 nm) were obtained on a Jasco 200D spectropolarimeter with an InSb detector using a 2 mm pathlength NIR quartz cuvette. Low-temperature CD and MCD spectroscopic experiments were performed using the Jasco spectropolarimeter, equipped with a modified sample compartment to accommodate focusing optics[47] and an Oxford Instruments Spectromag 4 superconducting (Oxford SM4-7T) magnet/cryostat. Protein samples (~0.2–0.4 mM) were prepared as anaerobic glasses in 66% (v/v) glycer(ol-d_3)/0.2 M sodium MOPS buffer plus 5% (^{1}H)-glycerol (pD 7.4). Samples were injected between two quartz discs separated by a 2–3 mm rubber spacer. Depolarization of the light by the MCD glass samples was monitored by their effect on the CD signal of a nickel (+)-tartrate solution placed before and after the sample.[48] In all cases, the depolarization was <10% at 4.2 K.

CD and MCD spectra were fit to Gaussian bandshapes using a constrained nonlinear least-squares fitting procedure. Each spectroscopic method has different selection rules, and although transitions can have different intensities, and in the case of CD and MCD different signs, the energies and bandwidths are the same. However, the low-temperature MCD spectra may have significantly sharper bandwidths and the band energies may shift slightly relative to the room temperature CD data, which was allowed for in the final fit.

Results

A. Fully Reduced MMOH. Figure 1 presents the room temperature near-IR CD and low-temperature MCD spectra of reduced MMOH from 5500 (the D_2O cutoff) to 12 500 cm^{-1}. The CD spectrum shows a broad negative feature at 10 000 cm^{-1} and a negative band centered at 7500 cm^{-1} both of which do not change position upon addition of glycerol and cooling to 4.2 K. The low-temperature MCD spectrum shows two positive transitions at ~7500 and 9000 cm^{-1} (shoulder) and one negative band at ~10 000 cm^{-1}. Gaussian spectral resolution can simultaneously fit both the CD and MCD spectra to three transitions at 7415 ± 100, 9140 ± 100, 9900 ± 100 cm^{-1} with only the sign and intensity of the peaks changing between the MCD and the CD spectra. The dashed lines in Figure 1 show the full Gaussian-resolved MCD spectrum.

B. Ligand Binding. The CD spectrum of fully reduced MMOH remains unchanged upon anaerobic addition of the small molecules N_3^-, CN^-, SCN^-, Cl^-, F^-, OCN^-, DMSO, imidazole, and acetonitrile. The concentration of the small molecules added to MMOH in the CD cell was varied up to a 50-fold molar excess relative to protein (1 mM MMOH). Addition of the enzymatic product methanol up to 2000-fold molar excess has no affect on the CD spectrum. Finally, addition of the substrate *trans*-1,2-dichloroethylene (2–3-fold molar excess) and the inhibitor tetrachloroethylene (3-fold molar excess) also result in no changes in the CD spectrum of the reduced hydroxylase. Representative spectra are shown in Figure 2. The lack of change in the CD spectrum does not appear to be due to incomplete saturation of the binding site. For example, the K_i value for tetrachloroethylene has been determined to be ~90 μM from steady-state kinetic studies.[46] Consequently, it is likely that MMOH was nearly saturated with this inhibitor under the conditions used here. Nevertheless, no change in the CD spectrum was observed.

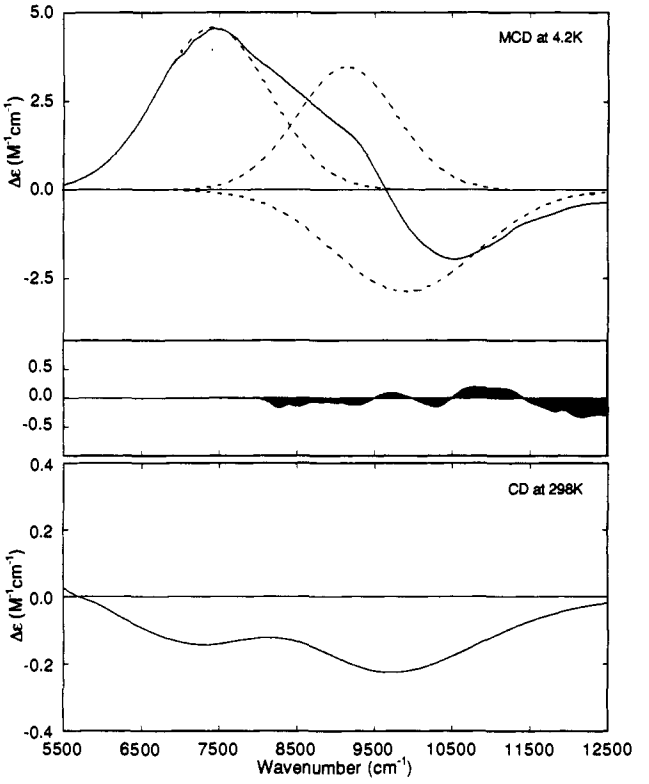

Figure 1. Low-temperature MCD (top) and room temperature CD (bottom) spectra of the binuclear non-heme Fe^{2+} active site in MMOH. The MCD spectrum was recorded at 4.2 K and 7.0 T. The raw MCD data was smoothed using a weighted fitting routine. The three ligand field transitions for MMOH are shown by Gaussian resolution of the MCD spectrum (– –). The difference spectrum is a plot of the smoothed MCD data minus Gaussian fit expanded by a factor of 10.

C. Fully Reduced MMOH with Component B. Figure 3 presents the MCD and CD spectra associated with the addition of a 4-fold molar excess of component B to the fully reduced hydroxylase. The room temperature near-IR CD spectrum (5500–12 500 cm^{-1}) shows one negative and one positive band centered at 7550 and 8800 cm^{-1}, respectively. Addition of glycerol to the MMOH–component B sample produced no change in the CD spectrum. The low-temperature MCD spectrum of the MMOH–component B complex displays a number of overlapping transitions in the region from 5500–10 000 cm^{-1} that can be Gaussian resolved into a minimum of three positive d → d transitions at 9800 ± 100, 7700 ± 100, and 6260 ± 100 cm^{-1}. Thus the low-energy CD band has a corresponding transition in MCD, but the 8800-cm^{-1} band remains unresolved in the MCD spectrum. Comparison between Figures 3 and 1 reveals that the MMOH–component B spectrum has three bands at approximately the same energy as MMOH and one additional low-energy feature.

D. Saturation–Magnetization. The MCD transitions for MMOH and MMOH–component B increase in signal intensity as temperature decreases indicating that these transitions are MCD C-terms. Thus the ground state of the fully reduced hydroxylase and the hydroxylase–component B complex are

(46) Fox, B. G.; Borneman, J. G.; Wackett, L. P.; Lipscomb, J. D. *Biochemistry* **1990**, *29*, 6419–6427.
(47) Spira-Solomon, D. J.; Allendorf, M. D.; Solomon, E. I. *J. Am. Chem. Soc.* **1986**, *108*, 5318–5328.
(48) Browett, W. R.; Fucaloro, A. F.; Morgan, T. V.; Stephens, P. J. *J. Am. Chem. Soc.* **1983**, *105*, 1868–1872.

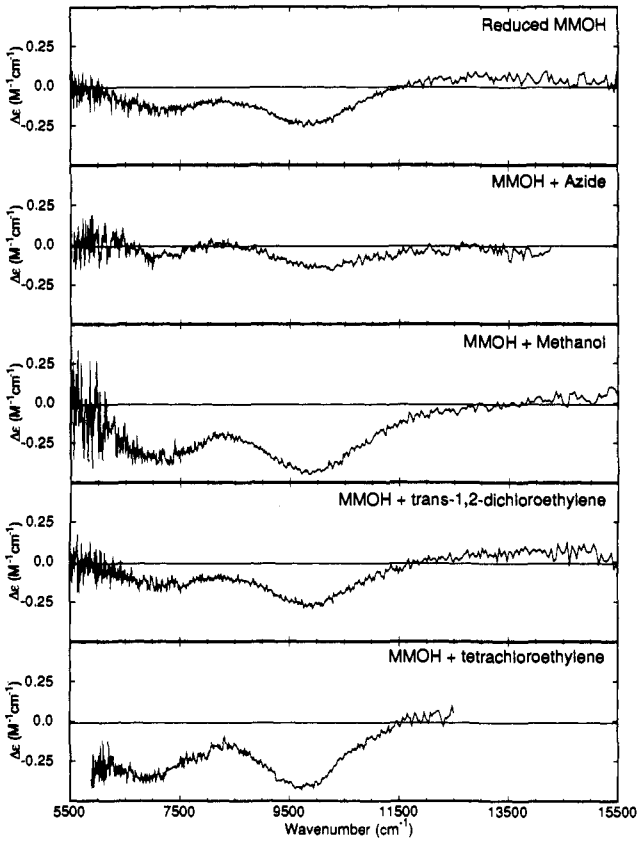

Figure 2. Small molecule, product, substrate, and inhibitor interactions with MMOH: room temperature CD spectra. The small intensity differences in the spectra result from heterogeneities in sample preparation (i.e., degree of protein denaturation or oxidation).

paramagnetic doublets which split in energy in a magnetic field. The field saturation curves measured on the positive band at 7575 cm^{-1} for MMOH and at 7750 cm^{-1} for MMOH–component B are shown in Figure 4 (parts A and B, respectively). The saturation curves obtained at increasing temperature when plotted as a function of the reduced parameter $\beta H/2kT$ do not superimpose, but are nested, a behavior observed for other metal sites with $S > {}^1/_2$ and associated with zero field splitting of the ground state.[49] In addition to nesting, the magnetization curves of both the reduced hydroxylase and the hydroxylase–component B complex show rapid saturation with the MMOH–component B complex saturating somewhat more quickly than MMOH, that is, at lower fields for the same temperature (note the expanded $\beta H/2kT$ scale in Figure 4B).

Also included for comparison in Figure 4 are the VTVH curves for deoxyN_3-Hr taken at 10 600 cm^{-1} (Figure 4C). These saturation–magnetization curves are also nested, since the high temperature curves are offset from the lowest temperature data. All curves between 4.2 and ~16 K lie above the lowest temperature data, while at temperatures greater than 16 K all the curves lie below the lowest temperature data.

Analysis

A. Ground-State Energy Splittings. As mentioned above, the saturation–magnetization curves in Figure 4 are nested with the high-temperature data offset from the low-temperature data. In addition, at lowest temperature and high fields the intensity increases linearly with increasing field. A pure C-term will saturate at low-temperature and high field, thus such MCD intensity behavior indicates the additional presence of a MCD B-term.

(49) Thomson, A. J.; Johnson, M. K. *Biochem. J.* **1980**, *191*, 411–420.

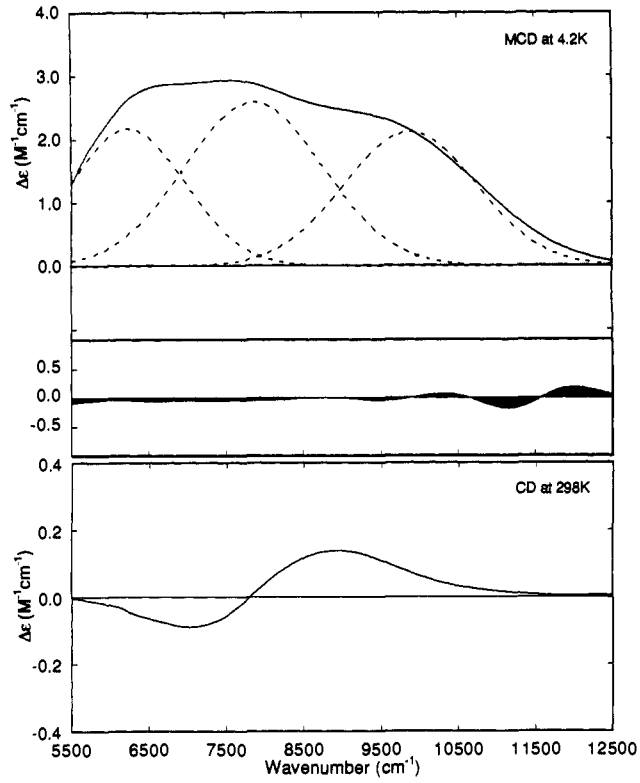

Figure 3. Low-temperature MCD (top) and room temperature CD (bottom) spectra of the binuclear non-heme Fe^{2+} active site in the MMOH–component B complex. The MCD spectrum was recorded at 4.2 K and 7.0 T. The raw data was smoothed using a weighted fitting routine. The three ligand field transitions for the component B complex are shown by Gaussian resolution of the MCD spectrum (– –). The difference spectrum is a plot of the smoothed MCD data minus Gaussian fit expanded by a factor of 10.

The expression for MCD intensity of an isolated zero-field split non-Kramers doublet[50] has been modified to include the effects of B-terms and low-lying excited states and is given in eq 1:

$$I = \int_0^1 \left(\sum_i \frac{A_i \cos^2 \Theta}{((\delta_i/(g_{\parallel_i}\beta H))^2 + \cos^2 \Theta)^{1/2}} \alpha_i \right) \mathrm{d} \cos \Theta + \sum_i B_i H \gamma_i \quad (1)$$

where

$$\alpha_i = \frac{\exp - [(E_i - {}^1/_2(\delta_i^2 - (g_{\parallel_i}\beta H \cos \Theta)^2))/kT]}{[\sum \exp - (E_j - {}^1/_2(\delta_j^2 - (g_{\parallel_j}\beta H \cos \Theta)^2))/kT]}$$

and

$$\gamma_i = \frac{\exp - (E_i/kT)}{\sum - (E_j/kT)}$$

In eq 1, I is the MCD intensity, A_i the MCD C-term intensity of state i, E_i the energy above the ground state ($E_1 = 0$), δ_i is the zero field splitting of the ith non-Kramers doublet, Θ is the angle between $g_\parallel$ and the external magnetic field H, T is the absolute temperature, and the constants β and k are the Bohr magneton and Boltzmann's constant, respectively. In this equation it is assumed that the transition is purely xy polarized and thus $g_\perp$ does not affect the MCD intensity. Each B_i will be the sum of

(50) Whittaker, J. W.; Solomon, E. I. *J. Am. Chem. Soc.* **1988**, *110*, 5329–5339.

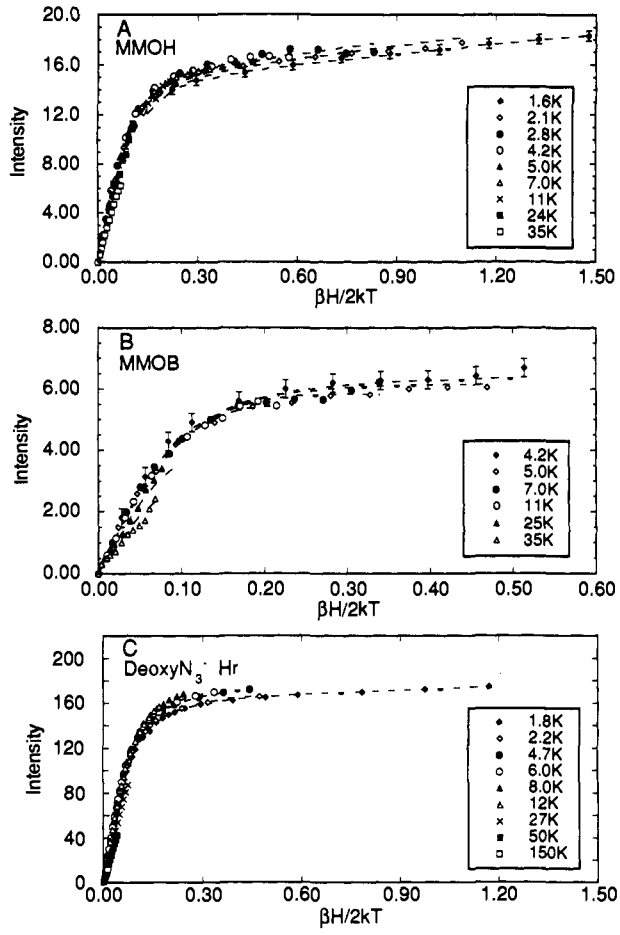

Figure 4. Saturation–magnetization behavior for (A) MMOH at 1320 nm, (B) MMOH–component B complex at 1290 nm, and (C) deoxyN_3-Hr at 940 nm. The MCD intensity amplitude for a range of magnetic fields (0–7.0 T) at a series of fixed temperatures is plotted as a function of $\beta H/2kT$. The fit to the VHVT MCD data (– –) is for the parameters shown in Table I and was obtained as described in the text. The error bars for the lowest temperature points have been included and are representative of the error for all the data points. In the case of deoxyN_3-Hr, the error bars for individual points are on the order of the symbol size used.

several B-terms arising from field induced mixing of the ith state with high-lying excited states as well as with other sublevels within the ground-state spin manifold. Values of A_i, δ_i, and $g_{\parallel i}$ are obtained by using a simplex routine to fit the experimental magnetization data sets in Figure 4, which consist of the MCD intensity, temperature, and the applied magnetic field strength.

The 1.7 and 2.0 K saturation–magnetization data of deoxyN_3-Hr lie on the same curve requiring that no other states are populated at low temperature. Application of eq 1 to these data using a single state (i = 1) reproduced the ground-state results obtained by Reem and Solomon,[30] in that deoxyN_3-Hr is ferromagnetically coupled with a $|4,\pm4\rangle$ (S_{Tot}, $M_{S_{Tot}}$) doublet lowest in energy (these states of the dimer are described in section B of the analysis) and $g_\parallel = 16.7\ cm^{-1}$. Furthermore, δ which measures the zero field splitting of the ±4 non-Kramers doublet has a value of $\sim 1.1\ cm^{-1}$. Ground-state analysis of the pumped helium temperature data of reduced MMOH indicates that there is a doublet lowest in energy which has a $g_\parallel = 14.7$ and $\delta < 1.0\ cm^{-1}$. Thus the site is also weakly ferromagnetically coupled consistent with the results in ref 44. Addition of component B to the fully reduced hydroxylase produces a change in the $g_\parallel$ value of the ground state of the binuclear ferrous site. The MMOH–component B complex is also ferromagnetically coupled and δ is again smaller than 1.0 wavenumber but it has a $g_\parallel \sim 16.1$. The ground-state parameters for deoxyN_3-Hr, MMOH, and MMOH–component B complex are given in the first two rows of Table I.

Table I. MCD Parameters for the Ground State and Lowest Excited States of deoxyN_3-Hr, MMOH, and MMOH–Component B Complex

	deoxyN_3-Hr	MMOH	MMOH–component B
$g_\parallel$	16.7 ± 0.5	14.7 ± 0.3	16.2 ± 0.6
δ (cm^{-1})	1.1 ± 0.4	<1.0	<1.0
$g_\perp$	2.7 ± 1.0	0.12 ± 0.1	0.09 ± 0.1
M_z/M_{xy}	0.04 ± 0.02	0.09 ± 0.03	~0.0
A_1	330.0 ± 2.0	29.2 ± 0.5	12.1 ± 0.1
B_1	1.78 ± 0.1	0.55 ± 0.01	0.11 ± 0.01
ES (cm^{-1})	30.0 ± 5.0	8.0 ± 2.0	5.0 ± 1.0

In order to validate the assumptions made in eq 1, namely that the electronic transitions are purely xy-polarized, the contribution of a z-polarized transition ($M_z/M_{xy} > 0$) and the consequent effects of a nonzero $g_\perp$ value have been investigated. In this approach, MCD C-term intensity is calculated by transforming the effective spin Hamiltonian for the lowest energy non-Kramers doublet to the complex basis, augmenting it with a perpendicular Zeeman term and numerically evaluating and averaging the spin Hamiltonian over angles using a Simpson's type approximation[51] as described in ref 50. A MCD B-term for the non-Kramers ground state has also been included in this analysis. The number of adjustable parameters required to fit the low-temperature saturation magnetization data is raised since $g_\perp$ and M_z/M_{xy} now contribute along with intensity (A), $g_\parallel$, δ, and B. Increasing the number of adjustable parameters from four to six would be expected to improve the quality of the fit relative to the fit from eq 1. However, no significant improvement is observed, indicating that the data do not require the additional parameters and that the transition studied is mostly xy polarized. Included in Table I are the resultant values for the additional parameters $g_\perp$ and M_z/M_{xy}.

Application of eq 1 to our earlier deoxyN_3-Hr saturation data allows the data from 1.7 to ~16 K to be fit with a single non-Kramers doublet having the ground-state parameters given in Table I. This analysis now includes the effects of a non-Kramers doublet and a B-term contribution not included in ref 30. At temperatures above ~20 K the non-Kramers ground state contribution alone does not fit the data, indicating population of an excited state (Figure 5A inset). In contrast, for MMOH and the MMOH–component B complex the ground-state parameters given in Table I can only be used to fit data up to 4.2 K. At higher temperatures, the fit consistently overestimates the intensity of the signal (Figure 5 (parts B and C inset)), indicating the presence of at least one low-lying excited state.

Application of eq 1 can now be extended to include the effects of excited states ($i > 1$) on the MCD saturation–magnetization curves. There are two possible excited states; a MCD active state (4,±3) (S_{Tot}, $M_{S_{Tot}}$) and a MCD inactive state (4,0;3,0) (vide infra). The (4,±3) doublet has an associated $g_\parallel$ value of 12, while for the (4,0;3,0) doublet $g_\parallel \sim 0$. Both doublets were considered as possibilities for the excited state in eq 1 {(4,±3): $|A_2| > 0$, $g_\parallel = 12$; (4,0;3,0): $A_2 = 0$, $g_\parallel = 0$)} allowing all the other parameters (B_2, δ_2, energy (E_i)) to vary.

Equation 1 with each possible excited state was applied to the deoxyN_3-Hr, MMOH, and MMOH–component B complex VTVH MCD data in Figure 5, and in each case the (4,±3) excited-state doublet gave a significantly better fit to the data (χ^2 decreased by 30%). In deoxyN_3-Hr, either excited-state doublet fits data up to 37 K well, but at higher temperatures the (4,0;3,0) doublet excited state fit overestimates the signal intensity. Therefore, the saturation fit for deoxyN_3-Hr requires the presence of an MCD active doublet at ~36 cm^{-1}. Allowing the MCD inactive doublet to be the excited state for MMOH does not give an appreciably better fit to the saturation data than did the ground-

(51) Press, W. H.; Flannery, B. P.; Teukolsky, S. A.; Vetterling, W. T. In *Numerical Recipes*, 3rd ed.; Cambridge University Press: Cambridge, 1988; pp 102–108.

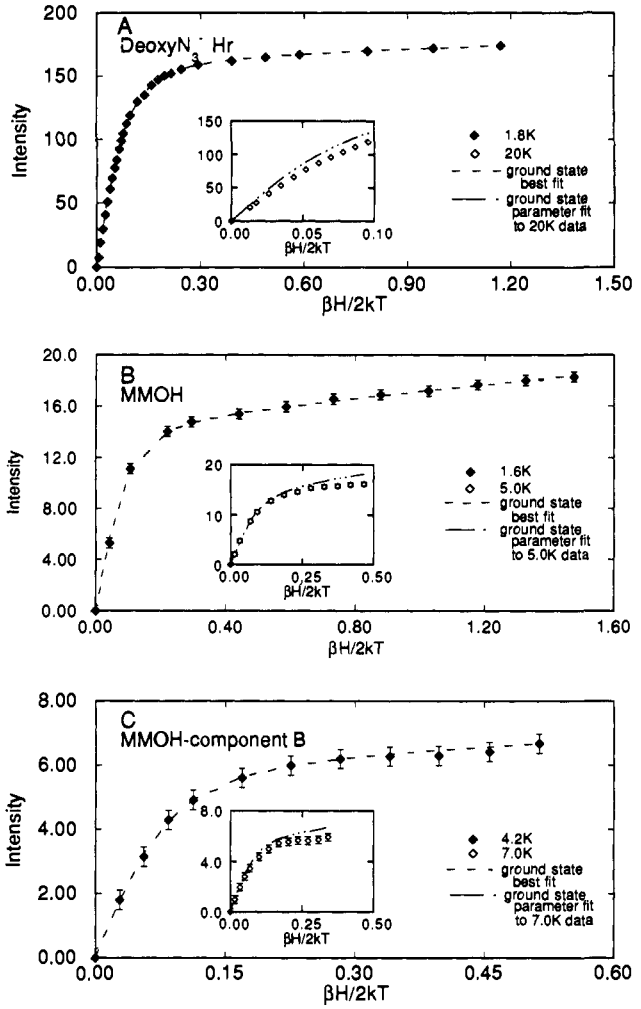

Figure 5. VH MCD (0.0–7.0 T) for (A) deoxyN_3-Hr at 940 nm and 1.8 K, (B) MMOH at 1320 nm and 1.6 K, and (C) MMOH–component B complex at 1290 nm and 4.2 K. The dashed curve represents the fit for an isolated non-Kramers doublet ground state. Higher temperature data cannot be accurately fit with the same parameters as the ground state data, as shown in the insets. Error bars have been included; in the case of deoxyN_3-Hr the error bars for individual points are smaller than the symbol size used.

state analysis described above. However, positioning the (4,±3) doublet at ~6.0 cm^{-1} produces a good fit to the MMOH data up to 50 K. In the case of the MMOH–component B complex, it is again the MCD active doublet excited state that is required for the best fit to the data. The (4,0;3,0) doublet state is able to fit data up to 11 K but at higher temperature the fit diverges from the data. When the (4,±3) doublet is set as the excited state a good fit to the complete VTVH MCD data set is obtained.

Finally we considered the effects of also including the (4,0;3,0) doublet state on the position of the (4,±3) doublet. In this case, eq 1 incorporates three states where the $g_\parallel$ value of the (4,±3) and the A and $g_\parallel$ values of the (4,0;3,0) state are fixed as described above, and all the remaining parameters are varied. The energy of the MCD inactive state was varied from 20 to 100 cm^{-1} with respect to the (4,±3) doublet in deoxyN_3-Hr and from −3 to 20 cm^{-1} for MMOH and the MMOH–component B complex. The results of this analysis for MMOH, MMOH–component B, and deoxyN_3-Hr are summarized in Figure 6.

In the case of MMOH, the single state analysis predicted the (4,±3) MCD doublet excited state to be ~6 cm^{-1} above the (4,±4) ground state. Setting the MCD inactive level at 3.0 cm^{-1} causes the fit to underestimate signal intensity at low fields and retains the MCD active state at approximately 6 cm^{-1}. As the inactive level is raised to 15 cm^{-1}, the (4,±3) doublet also increases in energy; however, the calculated curve deviates from the data at low-temperature and high fields. Best fit values are obtained when both the MCD active and the MCD inactive doublets are between 7 and 10 cm^{-1}. The fit to the complete set of MCD saturation–magnetization data with these excited states is given in Figure 4A. It is difficult to determine which is the lower excited state since the wave functions mix with rhombic distortion (vide infra). The eigenvectors associated with the (4,0;3,0) doublet have an appreciable contribution from $M_{S_{Tot}} = \pm 2$. Therefore, the MCD intensity and $g_\parallel$ value of this doublet can deviate from zero. Similarly, the eigenvectors of the (4,±3) doublet have contributions from $M_{S_{Tot}} = \pm 1$ with rhombic mixing. However, the VTVH MCD data require a MCD active excited state at ~7 cm^{-1}, and the fit is clearly improved (χ^2 decreased by 40%) with the addition of a third state at similar energy.

Application of this protocol to the MMOH–component B complex reveals limited differences in the parameters relative to those of reduced MMOH. As stated above, when only one excited state is considered, it is the MCD active (4,±3) doublet at ~9.0 cm^{-1} that gives the best fit to the VTVH MCD data. However, inclusion of the MCD inactive (4,0;3,0) doublet at ~5.0 cm^{-1} results in a better fit to the data and places the (4,±3) doublet at ~12.0 cm^{-1}. Raising or lowering the energy of the inactive doublet causes the calculated saturation curves to deviate from the experimental data at high fields. The resulting energy level diagram is given in Figure 6 (right) and this three-state fit to the complete saturation–magnetization MCD data is included in Figure 4B.

Finally, we have used this protocol to extend our analysis of deoxyN_3-Hr. Using either the (4,±3) or the (4,0;3,0) doublet as the excited state (at 25 and 36 cm^{-1}, respectively) gives good fits to the data up to 37 K, but only the MCD active (4,±3) excited state fits the data between 50 and 150 K. Including both excited states causes these energy levels to shift. If the MCD inactive doublet is placed much below 25 cm^{-1} with the (4,±3) doublet remaining at ~35 cm^{-1}, the calculated fit underestimates intensity at low fields and overestimates intensity at high fields. The best fit to the saturation magnetization curves is obtained when both the (4,0;3,0) and the (4,±3) levels are between 30 and 50 cm^{-1}. The energy level diagram is given in Figure 6 (left) and the fit to the complete set of VTVH MCD data for deoxyN_3-Hr is given in Figure 4C.

The above analysis assumes a (4,±3) state with $|A| > 0$ and $g_\parallel = 12$ and a (4,0;3,0) state with $A = 0$ and $g_\parallel = 0$. If these restrictions are removed and all parameters associated with a single excited state (A, B, $g_\parallel$, δ, and energy) are allowed to float, the following results are obtained: (1) MMOH requires an excited state between 6–9 cm^{-1} in order to fit the high temperature variable field saturation data; (2) the MMOH–component B complex saturation analysis gives an excited state at ~9.0 cm^{-1}; and (3) the first excited state of deoxyN_3-Hr is ~25 cm^{-1} above the ground state. In all these fits the excited state is MCD active, and the energies obtained are in reasonable agreement with those given in Figure 6.

B. Spin Hamiltonian Parameters. In order to interpret the MCD results summarized in Figure 6, we consider the electronic structure of the ground state of a coupled binuclear ferrous system. This is described by the spin Hamiltonian given in eq 2 where the subscripts denote the different Fe(II) ions.[30]

$$\mathcal{H} = -2J\hat{S}_1\cdot\hat{S}_2 + D_1(\hat{S}^2_{z1} - {}^1/_3S(S+1)) + E_1(\hat{S}^2_{x1} - \hat{S}^2_{y1}) + D_2(\hat{S}^2_{z2} - {}^1/_3S(S+1)) + E_2(\hat{S}^2_{x2} - \hat{S}^2_{y2}) + g_{z1}\beta H_z\hat{S}_{z1} + g_{x1}\beta H_x\hat{S}_{x1} + g_{y1}\beta H_y\hat{S}_{y1} + g_{z2}\beta H_z\hat{S}_{z2} + g_{x2}\beta H_x\hat{S}_{x2} + g_{y2}\beta H_y\hat{S}_{y2} \quad (2)$$

Equation 2 includes the exchange coupling (J) between the iron ions, the axial ($D_{1,2}$) and rhombic ($E_{1,2}$) zero-field splitting (ZFS) parameters for each iron (1,2), and Zeeman terms ($g_{z1}\beta H_zS_{z1}$,

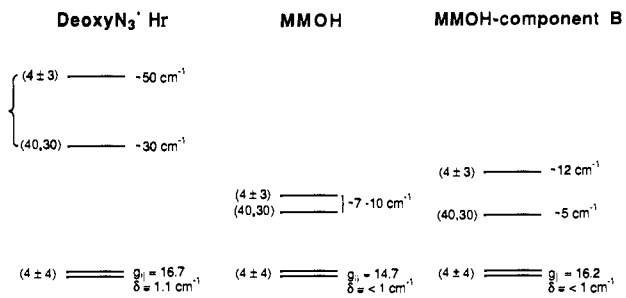

Figure 6. Energy level diagrams for deoxyN$_3$-Hr, MMOH, and the MMOH–component B complex summarizing the best fit to the complete VTVH MCD data. Brackets indicate an upper and lower limit for the excited states.

etc.) where the single site $g_{Fe^{2+}}$ can be coupled to the ZFS parameters using ligand field theory as described in eqs 3a and b.[52] This Hamiltonian operates on an uncoupled basis set $|S_1,M_{s1}, S_2,M_{s2}\rangle$ yielding a 25 × 25 matrix. Diagonalization of this matrix in zero field with $D_1 = D_2$ and $E_1 = E_2 = 0$ gives the energy level diagrams shown in Figure 7 where A corresponds to antiferromagnetic ($J < 0$) and B to ferromagnetic ($J > 0$) coupling.

$$D_{Fe^{2+}} = \frac{-k^2\lambda_o}{4}(g_{xFe^{2+}} + g_{yFe^{2+}} - 2g_{zFe^{2+}}) \quad (3a)$$

$$E_{Fe^{2+}} = \frac{-k^2\lambda_o}{4}(g_{yFe^{2+}} - g_{xFe^{2+}}) \quad (3b)$$

The energy levels that result when there is no exchange coupling are shown at the right of Figure 7A.[53] These states are labeled by the uncoupled basis functions on the two irons (M_{s1}, M_{s2}). Allowing the iron atoms to interact corresponds to J increasing to the left in the diagram and splits the energy of these levels. The left side of Figure 7A shows the limiting case with large exchange coupling and no axial ZFS. In this limit, two $S = 2$ ions are antiferromagnetically coupled to produce five multiplets having the spin values $S_{Tot} = 0$–4. These levels split into singlets and doublets when D is included, moving toward the middle of the diagram. The singlets and doublets that result are labeled by the dominant contribution in the coupled spin wave functions (S_{Tot}, M_s). As the magnitude of J and D become comparable, the splitting and mixing of the levels becomes increasingly more complicated. Our earlier temperature and field dependent MCD data on deoxyHr indicated that the ground state is MCD inactive but that a paramagnetic state is populated at higher temperatures.[30] Both the right and left sides of Figure 7A could be used to fit the deoxyHr data; however, in the limit of $D > 0$ and $J = 0$ (right side), the Fe(II) ZFS parameter would be required to be ~35 cm^{-1} which is larger than the maximum reasonable value of $D \sim 15$ cm^{-1}.[54] In the limit of $-J > 0$ and $D = 0$ (left side) the location of the MCD active excited state would give a $-J$ value of ~25 cm^{-1}. However, this requires that the ferrous ZFS parameter and the exchange coupling constant be of similar magnitude, and thus both effects must be included in a quantitative fit to the deoxyHr MCD data (center of Figure 7A). This resulted in $12 < -J < 38$ cm^{-1} for deoxyHr.[30]

In contrast, the VTVH MCD data for deoxyN$_3$-Hr indicate that the ground state is a MCD active doublet with a $g_\parallel \sim 16$. Therefore for deoxyN$_3$-Hr the two ferrous centers are weakly ferromagnetically coupled which corresponds to a positive value of J. Figure 7B treats the ferromagnetic case by allowing for effects of varying the axial ZFS. Both axes are in units of J, so that this parameter is also allowed to vary. If $D < 0$ (left side) the $|4,\pm4\rangle$ non-Kramers doublet is the ground state with the $|4,\pm3\rangle$ doublet or the $|4,0\rangle$ and $|3,0\rangle$ singlet states at higher energy depending on the magnitude of $-D/J$.[55] Alternatively, if $D > 0$ the ground state is a singlet for any value of D and would not show MCD C-term intensity at lower temperatures. The $g_\parallel \sim 16$ observed in deoxyN$_3$-Hr requires ferromagnetic exchange coupling and negative ZFS between the Fe(II) ions, giving an $M_s = \pm4$ ground state (bottom left).[30]

Inclusion of a rhombic perturbation on the energy level diagram in Figure 7B gives Figure 7C for $D_1 = D_2$ and $E_1/D_1 = E_2/D_2 = {}^1/_3$ (the rhombic limit) in eq 2. The remaining degeneracies are removed as the $M_s = \pm n$ doublets are split and the wave functions mix. It is interesting to note that the ground-state ±4 doublet shows only a small splitting even at the maximum rhombic limit. The VTVH MCD parameter δ in eq 1 is a measure of this rhombic splitting of the $M_s = \pm4$ doublet. Fitting eq 2 to the experimental values of δ, $g_\parallel$, and the energy of the first excited state summarized in Table I allows values for the spin Hamiltonian parameters to be obtained. All fits discussed below are constrained such that $E_1/D_1 = E_2/D_2 = {}^1/_3$ and the ZFS tensors are colinear.

The saturation–magnetization ground-state parameters for deoxyN$_3$-Hr summarized in Table I and Figure 6 were used to determine the spin Hamiltonian parameters in eq 2. Recalling that the first excited state for deoxyN$_3$-Hr lies at 30 cm^{-1} (Figure 7B), we are able to limit the range of possible J, D solutions. In order to extract the ground-state parameters all values of D and J resulting in an excited state 25–35 cm^{-1} above the ground state were located. The results are given in Figure 8A, where the solid and dashed curves bracket the values of J and D required to reproduce the experimental splitting range of 25–35 cm^{-1}. Similarly, VTVH MCD fits determined the value for the zero-field splitting of the non-Kramers doublet ground state, δ, to be 1.1 cm^{-1}. D and J values in eq 2 that give a δ value between 0.5 and 1.5 cm^{-1} are also given in Figure 8A (– ··· – and – · –). Figure 8A presents a solution space for deoxyN$_3$-Hr in terms of J and D. The region shown in Figure 8A is consistent with the qualitative discussion of the saturation–magnetization data presented earlier; $J > 0$ corresponding to ferromagnetic coupling, and $D < 0$ corresponding to the $(4,\pm4)$ ground state. Note that the curves giving the solutions to the excited-state energy consist of two regions: one dependent on J but independent on D (flat), and the other only dependent on D (steep). The former corresponds to the (4,0;3,0) excited-state doublet as the first excited state, while the latter coincides with the $(4,\pm3)$ doublet, and therefore the intersection of the curves signifies the crossing of the (4,0;3,0) and $(4,\pm3)$ energy levels in Figure 7B.

From Figure 8A the magnitudes of J and D are constrained to a limited region in solution space in order to fit both the first excited-state and the zero-field splitting data. J values range from 1.6 to 2.4 cm^{-1}, while $D_1 = D_2$ are constrained to lie between –12 and –25 cm^{-1}. However, from ligand field theory the largest reasonable magnitude for the ZFS should be observed in a distorted six-coordinate Fe(II) site and is experimentally found to be approximately –15 cm^{-1} [54,56] which places an additional constraint on the solution in Figure 8A. From VTVH MCD data, $g_\parallel$ is determined to be 16.7 ± 0.5. Figure 8B presents the $g_\parallel$ values obtained over a range of J and D values. Values of $g_\parallel > 16.5$ can only be obtained if $J > 1.0$ cm^{-1}. As J increases to 5 cm^{-1} the range of D values becomes –7 to –15 cm^{-1}. Thus the experimental $g_\parallel$ of 16.7 is in agreement with the region of solution

(52) For the plots shown in Figures 7 and 8 g_x was held equal to 2.00, and the other $g_{Fe^{2+}}$ were determined using eq 3. The Fe^{2+} spin orbit coupling constant λ_o was set equal to –100 cm^{-1}, and k^2, the Stevens orbital reduction factor, set equal to 0.8.

(53) Note that the right hand side of Figure 7A can be used to describe a system with ferromagnetic coupling between two Fe(II) ions each with negative ZFS by reversing the energy scale such that the $(\pm2,\pm2)$ state becomes the ground state. This description corresponds to the perturbation treatment presented in Figure 4 of ref 44.

(54) Rudowicz, C. *Acta Phys. Pol.* **1975**, *A47*, 305–321.

(55) Note that we use a coupled basis set to describe the wave functions in Figure 7B. However, as D becomes comparable or larger than J only M_s is a good quantum number, and the wave functions in the coupled basis set mix such that, for example, the states labeled $|4,0\rangle$, $|3,0\rangle$ are each a combination of all S_{Tot} states with $M_s = 0$.

(56) Champion, P. M.; Sievers, A. J. *J. Chem. Phys.* **1977**, *66*, 1819–1825.

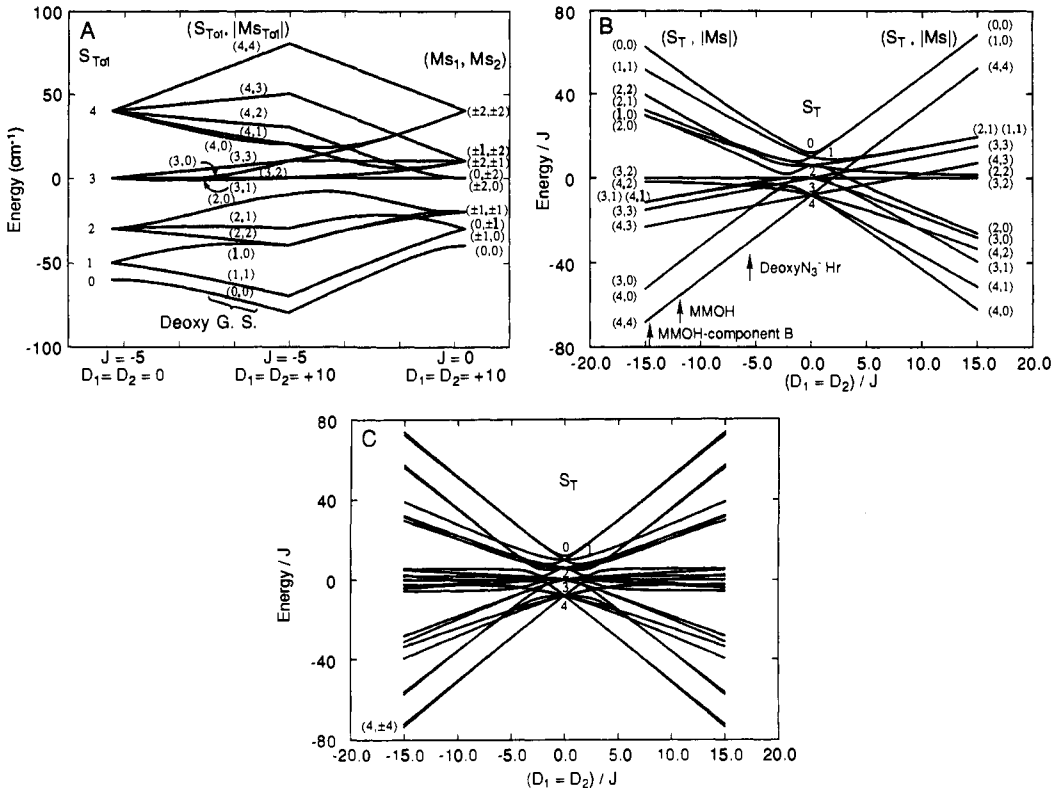

Figure 7. Correlation diagram of the energy levels of the binuclear ferrous ground state including exchange coupling and single-site ZFS. In (A) the left side is the limit of only antiferromagnetic coupling between two $S = 2$ ions, with multiplets labeled by the total spin of the dimer (S_{Tot}). The right side gives the pure ZFS limit with states labeled with M_s values for each uncoupled Fe(II) (M_{s1}, M_{s2}). The central portion shows the splitting when both ZFS and exchange coupling are present with states labeled using the coupled basis (S_{Tot}, $M_{s_{Tot}}$) describing the dominant contribution to the dimer wave functions. In (B) the states are plotted in reduced variables with the ordinate being (Energy/J) and the abscissa showing variation of ZFS (D/J). The exchange coupling (J) is held constant, and the axial ZFS parameters on the two Fe(II) atoms are constrained to be equal and range from $-15J$ to $15J$. The spin Hamiltonian used for calculating the levels is given in eq 2, with $E_1 = E_2 = 0$. (C) gives the energy levels of the binuclear ferrous ground state described in (B) at the rhombic limit of $E/D = 1/3$.

space indicated in Figure 8A. If the axial ZFS parameters for the two iron atoms are allowed to become unequal, a fit to the data is obtained if J is 2.0 ± 0.4 cm^{-1} and D_1 and D_2 both range from −12 to −15 cm^{-1}. Therefore for deoxyN$_3$-Hr, $1.6 < J < 2.4$ cm^{-1} and $-15.0 < D_1, D_2 < -12.0$ cm^{-1}. From Figure 8A, these parameters predict the (4,0;3,0) doublet to be the first excited state in Figure 7B but with the 4±3 close in energy which is consistent with VTVH MCD data.

Figure 8C presents the solution space for MMOH in terms of J and D. The ground-state parameters for MMOH given in Table I and Figure 6 were used to establish limiting excited-state energies of 5 cm^{-1} (solid) to 12 cm^{-1} (dashed) as well as an upper limit for δ of 1.0 cm^{-1} (the lower limit of 0.2 cm^{-1} is given by EPR data[44]). One should note that the solution space for MMOH lies at both lower J and D ($D_1 = D_2$) values than the solution space for deoxyN$_3$-Hr. This indicates that MMOH is more weakly ferromagnetically coupled than deoxyN$_3$-Hr. The exchange coupling lies between 0.2 and 0.8 cm^{-1}, while the D values are constrained between −3 and −10 cm^{-1}. Incorporating $g_{\|} = 14.7$ into the analysis for MMOH places further limits on the solutions. From Figure 8D a $g_{\|} < 15.0$ is obtained when $J < 0.5$ cm^{-1}. From Figure 8C this upper limit on J reduces the range of consistent D values to −3 and −7 cm^{-1}.

Allowing the D values to become unequal results in a J between 0.3 and 0.4 cm^{-1}. The VTVH MCD fit parameters given in Table I are consistent with D_1 ranging from −2 to −15 cm^{-1} while D_2 is limited between −1 and −7 cm^{-1}. This range also accommodates the $g_{\|} < 15.0$ and predicts the first excited state to be between 6 and 9 cm^{-1}, which correlates with Figure 8C. From Figure 8C the first excited state is the (4,0;3,0) MCD inactive doublet, but Figure 7B predicts the (4,±3) doublet to be close in energy. Since the abscissa in Figure 7B is given as a reduced parameter (Energy/J), a small J gives closely spaced energy levels. These results are therefore consistent with the MMOH VTVH MCD analysis in section A which indicated that the (4,0;3,0) and (4,±3) doublets are at similar energies.

Figure 8C also presents the solution space for the MMOH–component B complex since the first excited state in the complex lies at ∼5 cm^{-1} and $\delta < 1.0$ cm^{-1}. Therefore the MMOH–component B complex, like MMOH, is more weakly coupled than deoxyN$_3$-Hr. The spin Hamiltonian analysis of the MMOH–component B complex MCD data shows that in the case of $D_1 = D_2$, a $g_{\|}$ of approximately 16 can only be obtained if $J > 0.5$ cm^{-1} and that the entire range of D are possible solutions. However, from Figure 8C the location of the (4,0;3,0) doublet as the first excited state at ∼5.0 cm^{-1} requires $J < 0.5$ cm^{-1}. The above results are contradictory, indicating that D_1 cannot equal D_2. When $D_1 \neq D_2$, all the saturation–magnetization parameters can be accommodated if both D_1 and D_2 decrease when compared to deoxyN$_3$-Hr. When D_1 ranges from −3 to −10 cm^{-1} and D_2 lies between −3 and −10 cm^{-1} but $D_1 \neq D_2$ and $0.3 < J < 0.5$ cm^{-1}, the first excited state is at ∼5.0 cm^{-1} and $g_{\|} \sim 16.0$ which agrees with the VTVH MCD parameters. Figure 8C predicts the (4,0;3,0) doublet as the first excited state which is consistent with the saturation magnetization analysis presented above. The VTVH MCD analysis also predicted that the first and second excited states in the MMOH–component B complex are split to a larger extent than in MMOH; therefore, the component B complex lies to the left of MMOH in Figure 7B. The results from the spin Hamiltonian analysis are summarized in Table II and graphically presented in Figure 7B in terms of the reduced parameter D/J for $D_1 = D_2$.

In summary, the spin Hamiltonian analysis confirms that deoxyN$_3$-Hr, MMOH, and the MMOH–component B complex

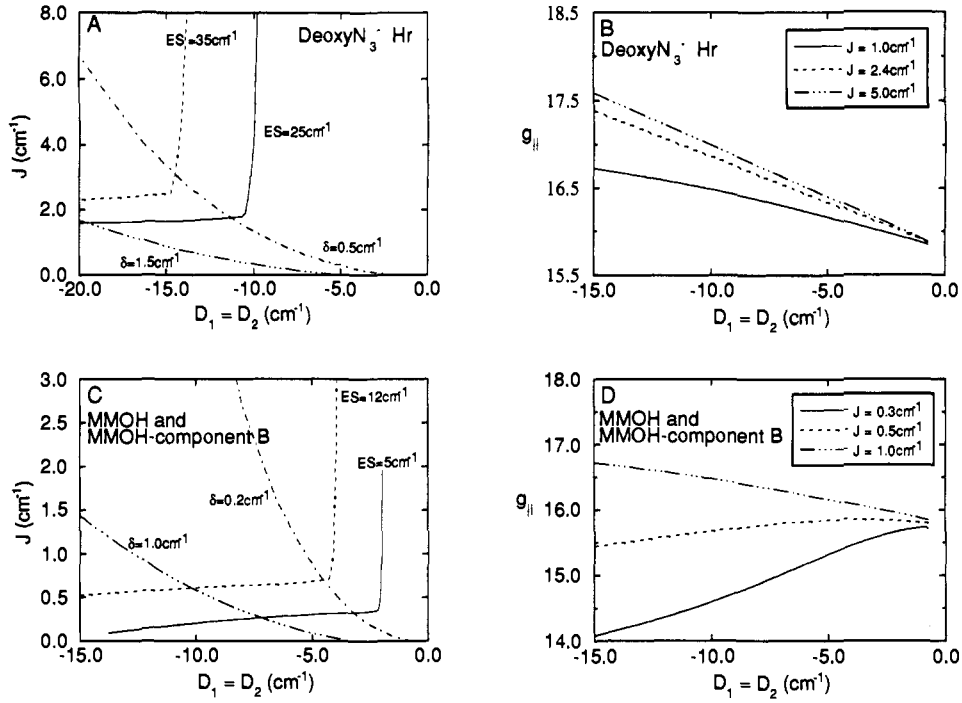

Figure 8. D vs J solution space for deoxyN$_3$-Hr, MMOH, and MMOH–component B in terms of δ, $g_\parallel$, and the energy of the first excited state (ES). (A) and (C) present curves showing the values of D and J which produce energy levels such that the first excited doublet is between 25 and 35 cm^{-1} or 5 and 12 cm^{-1} for deoxyN$_3$-Hr and MMOH/MMOH–component B, respectively. The axial ZFS parameters for the two iron atoms are constrained to be equal. (B) and (D) show the $g_\parallel$ values obtained over a range of J and $D_1 = D_2$ values for deoxyN$_3$-Hr and MMOH and the MMOH–component B complex, respectively.

Table II. Spin Hamiltonian Parameters for DeoxyN$_3$-Hr, MMOH, and MMOH–Component B Complex

	DeoxyN$_3$-Hr	MMOH	MMOH–component B
J (cm^{-1})	2.2 ± 0.4	0.3 ± 0.1	0.4 ± 0.1
D_1 (cm^{-1})[a]	−13.0 ± 2.0	−4.0 ± 3.0	−6.0 ± 3.0
D_2 (cm^{-1})[a]	−13.0 ± 2.0	−9.0 ± 6.0	−6.0 ± 3.0

[a] Note that these values represent a range for D_1 and D_2.

are all weakly ferromagnetically coupled and therefore require $J > 0$ cm^{-1} and $D_{1,2} < 0$ cm^{-1}. DeoxyN$_3$-Hr is more strongly coupled than the hydroxylase and the component B complex. The position of the first excited state also changes drastically between the different proteins. DeoxyN$_3$-Hr has a first excited state at ~30.0 cm^{-1}, whereas MMOH has two unresolvable levels between 7 and 10 cm^{-1}. The MMOH–component B complex also has two low-lying excited states, but these are more clearly separated than those of MMOH giving a first excited state at ~5.0 cm^{-1}. These changes in the excited-state energy levels manifest themselves in the spin Hamiltonian parameters (Table II). DeoxyN$_3$-Hr has two large negative D values which can be equal, indicating that both iron atoms have similar coordination environments. In the case of MMOH, at least one D value has greatly decreased, but the data cannot distinguish between a large or small value for the D of the second iron. Finally, the spin Hamiltonian analysis of the MMOH–component B complex indicates that both D values have decreased relative to deoxyN$_3$-Hr and that the lower limiting value of D is slightly larger than for MMOH.

The differences observed in the spin Hamiltonian analysis for deoxyN$_3$-Hr, MMOH, and the MMOH–component B complex provide insight into potential differences in active site geometry related to enzyme reactivity. Changes in the ZFS splitting parameter can be correlated to Fe(II) geometry (vide infra). Since deoxyN$_3$-Hr has two large negative D values and MMOH and the component B complex have at least one small negative D value, the coordination environment of the Fe^{2+} in the active site of deoxyN$_3$-Hr and MMOH must be different. The change from antiferromagnetism in deoxyHr to ferromagnetism in deoxyN$_3$-Hr was interpreted in terms of protonation of hydroxide to form a H_2O bridge.[30] From pulsed ENDOR and ESEEM studies,[57] as with half-met [Fe(II)Fe(III)]Hr, half-met MMOH has an OH^- bridge. The fact that both fully reduced MMOH and the MMOH–component B complex are ferromagnetic would indicate that the OH^- bridge is eliminated on reduction. This would involve protonation to give H_2O which either bridges or is lost from the site. Weak exchange coupling would also be expected for a binuclear ferrous center containing only μ-carboxylate bridges. The lower exchange coupling of MMOH relative to deoxyN$_3$-Hr results from either a change in the bridging ligands (deoxyN$_3$-Hr has two carboxylate bridges) or a change in the coordination environment of the Fe atoms, hence rotating the magnetic orbitals relative to the bridge.

C. Ligand Field Theory of Excited-State Energy Splittings. Figures 1 and 3 show that reduced MMOH has one low-energy band (7500 cm^{-1}), while the MMOH–component B complex has two transitions at low energy (6200, 7700 cm^{-1}). In order to gain insight into the geometry of each iron atom in the active site of MMOH and the MMOH–component B complex, one needs to evaluate which coordination environments would be consistent with the presence of such low-energy transitions for a ferrous center.

Theoretical energy levels and wave functions were calculated by using the method of Companion and Komarynsky.[58] In the electrostatic crystal field approximation, the ligands are treated as point charges which perturb the d electron energy levels removing their degeneracy in a manner dependent on the arrangement of the ligands around the metal ion. No simplifying assumptions about site symmetry are made, and each element of the secular determinant ($|H_{pq} - S_{pq}E_k| = 0$) is calculated using the real d orbitals (p and q) as the basis set. Since the real d orbitals are an orthonormal set, the integrals S_{pq} will be 1 when

(57) Thomann, H.; Bernardo, M.; McCormick, J. M.; Pulver, S.; Andersson, K. K.; Lipscomb, J. D.; Solomon, E. I. *J. Am. Chem. Soc.* **1993**, *115*, 8881–8882.

(58) Companion, A. L.; Komarynsky, M. A. *J. Chem. Ed.* **1964**, *41*, 257–262.

Table III. Ligand Field Parameters Determined for Structurally Defined Fe(II) Complexes

Fe–O or Fe–N bond length	type of O or N ligand	complex	α_2, cm^{-1}	α_4, cm^{-1}
2.23	pyridine	$Fe(py)_4Cl_2$[a]	18 000	5900
2.21	imidazole	$Fe(Im)_6$[b]	18 520	6170
2.17	imidazole	$Fe(Im)_6$[b]	19 850	7850
2.15	Me_6tren	$Fe(Me_6tren)Br$[c]	20 000	8000
2.14	H_2O	$Fe(H_2O)_6$[d]	18 700	5600
2.08	H_2O	$Fe(H_2O)_6$[d]	17 300	5760

[a] Long, G. L.; Clarke, P. J. *Inorg. Chem.* **1978**, *17*(6), 1394–1401. [b] Miller, L. L.; Jacobson, R. A.; Chen, Y.-S.; Kurtz, D. M. *Acta Crystallogr.* **1989**, *C45*, 527–529. [c] Vaira, D. M.; Orioli, P. L. *Acta Crystallogr.* **1968**, *B24*, 1269–1272. [d] Montgomery, H.; Chastain, R. V.; Natt, J. J.; Witkowska, A. M.; Lingafelter, E. C. *Acta Crystallogr.* **1967**, *22*, 775–780.

$p = q$ and 0 otherwise, therefore reducing the problem to the evaluation of the H_{pq} matrix elements. A general form for these matrix elements is given in eq 4

$$\langle\psi_p|H|\psi_q\rangle = \sum_i^N \sum_{\ell=0,2,4} \sum_{m=-\ell}^{\ell} \frac{4\pi Z_i e^2}{2\ell+1} Y_{\ell m}^*(\theta_i\phi_i) \int \psi_p^* \left[\frac{r_<^\ell}{r_>^{\ell+1}}\right]_i Y_{\ell m}(\theta,\phi)\psi_d d\nu \quad (4)$$

where N equals the total number of ligands (i), and ℓ and m are the quantum numbers of the spherical harmonics. The radial and angular parts of this integral can be separated and a quantity $\alpha_\ell{}^i$ defined such that

$$\alpha_\ell{}^i = Z_i e^2 \int_0^\infty R_{3d}{}^2 \left[\frac{r_<^\ell}{r_>^{\ell+1}}\right]_i r^2 dr \quad (5)$$

Given the spatial coordinates and values of α_0, α_2, and α_4 for each ligand, each of the elements of the secular determinant can be calculated. Diagonalization of the Hamiltonian matrix yields the five energy levels of the ferrous site.

Since the parameters $\alpha_0{}^i$ contribute equally to all of the diagonal elements of the matrix, they do not affect the energy splittings and are set to zero. A pure electrostatic crystal field model is known to give poor agreement with experiment for the values of radial integrals. In ligand field theory the values for $\alpha_2{}^i$ and $\alpha_4{}^i$ are determined experimentally through the use of model complexes.[59-61] Nitrogen and oxygen donor ligands are appropriate for MMOH and many other non-heme Fe^{2+} protein sites and are considered in this analysis. The complexes used as models all had X-ray crystallographically determined structures and are listed in Table III. The values of α_2 and α_4 were systematically varied for each model complex until the set which produced the best match between the calculated energy level splittings and the ligand field optical spectrum was obtained. The results are summarized in Table III.

The ligand field parameters calculated for the model complexes are appropriate only for the metal–ligand distances found in these complexes. However, from EXAFS data[39] an average Fe–N bond length is estimated to be 2.2 Å in fully reduced MMOH and an average Fe–O bond length is 2.08 Å, thus the α_2 and α_4 values listed in Table III can be used as reasonable approximations for the protein data. In addition, MMO has a higher oxygen coordination environment than Hr, although ENDOR studies on half-met MMOH[57,62] indicate that there is at least one histidine-N bonded to each iron in the hydroxylase active site. Therefore, the ligand field calculations described below were performed on complexes with mixed N/O ligand sets.

Ligand field calculations for six-coordinate Fe(II) geometries were performed first. The Fe(II) free ion has a ^5D state lowest in energy which splits in an octahedral field into a 3-fold orbitally degenerate $^5T_{2g}$ ground state and a 2-fold degenerate ^5E_g excited state. In the octahedral case this is the only spin allowed ligand field transition and is usually seen as an absorption band at 10DqOh, which is in the range of 10 000–11 000 cm^{-1} for O and N ligands.[59] The ^5E_g state in a six-coordinate Fe(II) complex is generally split either by an excited-state Jahn–Teller distortion or by a static low-symmetry distortion in the ground state, resulting in a pair of absorption transitions split by 1000–2000 cm^{-1} and centered around 10 000 cm^{-1}. Figure 9 presents the ligand field energy levels calculated for a range of pseudooctahedral six-coordinate Fe(II) geometries. Note that high-spin Fe(II) has four unpaired electrons, one in each d orbital plus an additional electron pair in the lowest energy orbital, therefore the orbital energy differences in Figure 9 give the observed ligand field transition energies (in the absence of electronic relaxation). The Fe^{2+} geometries were obtained from a variety of crystallographically characterized ferrous complexes represented pictorially on the top of Figure 9, but the ligand environment (one N and five O) was chosen to reflect the fact that MMOH has primarily oxygen donor ligands. The calculations agree with the general qualitative six-coordinate ligand field model presented above (see Figure 9) and indicate that the lowest energy band associated with a pseudooctahedral Fe(II) geometry is above 8100 cm^{-1}. Therefore, MMOH and the MMOH–component B complex have at least one Fe^{2+} which is less than six-coordinate since both show d → d transitions below 8000 cm^{-1}.

Since the parameters of ligand field theory are dependent on the nature of the metal and ligand and on the bond length but should not be dependent on coordination number or angle, the calculations discussed above can be extended to five-coordinate structures. As a calibration, the parameters in Table III adjusted for the experimental bond lengths were used to predict the ligand field transitions of a five-coordinate complex with known structure.[63] The splitting of the transitions were found to be in good agreement with experiment (within 200 cm^{-1}), while the absolute energy of the transitions was overestimated by <1500 cm^{-1}. Figure 10 presents the d orbital splitting and thus the ligand field transitions associated with pentacoordinate Fe(II) complexes using the bond lengths for the Fe in MMO obtained from EXAFS.[39] Removing one axial ligand from a tetragonally distorted O_h complex results in a large axial perturbation and leads to the formation of a five-coordinate complex that has the metal in the plane of the equatorial ligands (structure A in Figure 10). Five-coordinate ferrous complexes have much lower ligand field strengths than six-coordinate complexes with the two orbital components of the ^5E_g state split by greater than 2000 cm^{-1}.[64,65] The magnitude of the ^5E ($x^2 - y^2$ and z^2) splitting for structure A in Figure 10 is on the order of ~10 000 cm^{-1}. However, with only one axial ligand the metal will shift out of the equatorial plane toward the remaining axial ligand as in structure B of Figure 10, forming a square-pyramidal complex and reducing the ^5E splitting to ~7000 cm^{-1}. A square-pyramidal geometry can be distorted into a trigonal-bipyramidal structure (D_{3h}) via an intramolecular rearrangement known as the Berry pseudorotation.[66] Figure 10 includes a correlation diagram of this distortion of a five-coordinate ferrous site relating the C_{4v} (with

(59) Lever, A. P. B. In *Inorganic Electronic Spectroscopy*; Elsevier: New York, 1984; pp 458–467.
(60) *Part I. Electronic Structure of Transition Metal Complexes*; Avery, J., Dahl, J. P., Hansen, A. E., Eds.; Understanding Molecular Properties; D. Reidel Publishing Company: Dordrecht, 1987.
(61) Solomon, E. I.; Kirk, M. L.; Gamelin, D. G.; Pulver, S. In *Methods Enzymol.*, in press.
(62) Hendrich, M. P.; Fox, B. G.; Andersson, K. K.; Debrunner, P. G.; Lipscomb, J. D. *J. Biol. Chem.* **1992**, *267*, 261–269.
(63) Campochiaro, C.; Hagen, K. S.; Solomon, E. I., unpublished results.
(64) Nicholls, D. In *The Chemistry of Iron, Cobalt and Nickel*; Pergamon: New York, 1973; pp 979–1051.
(65) Clampolini, M.; Nardi, N. *Inorg. Chem.* **1966**, *5*, 1150–1154.
(66) Berry, R. S. *J. Chem. Phys.* **1960**, *32*, 933–938.

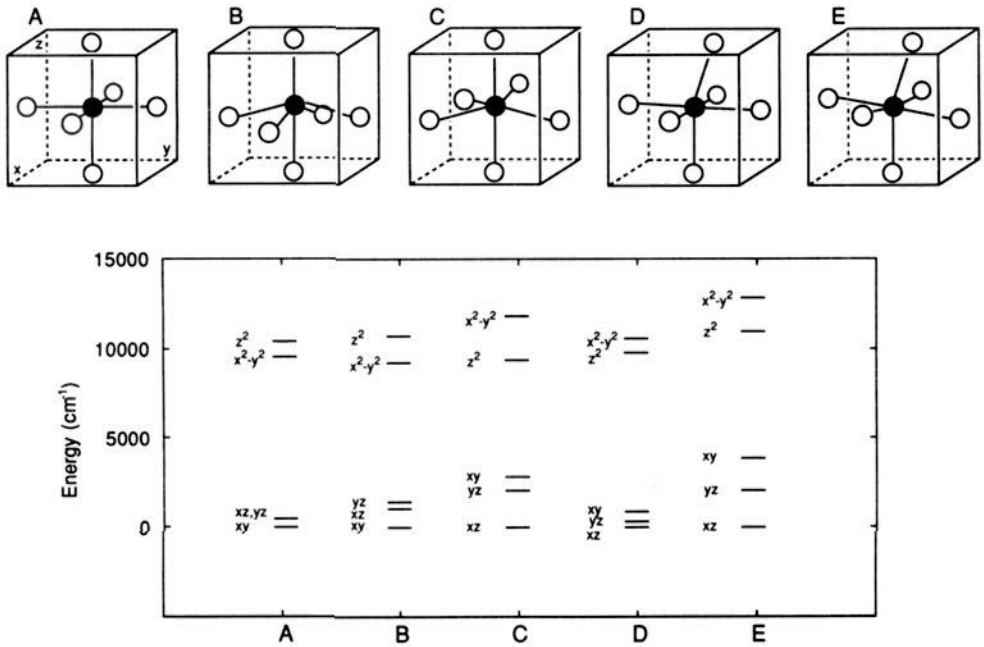

Figure 9. Calculated d orbital energy level diagrams for high-spin Fe(II) in octahedral and distorted octahedral geometries. Iron is represented as a filled sphere and ligands as open spheres.

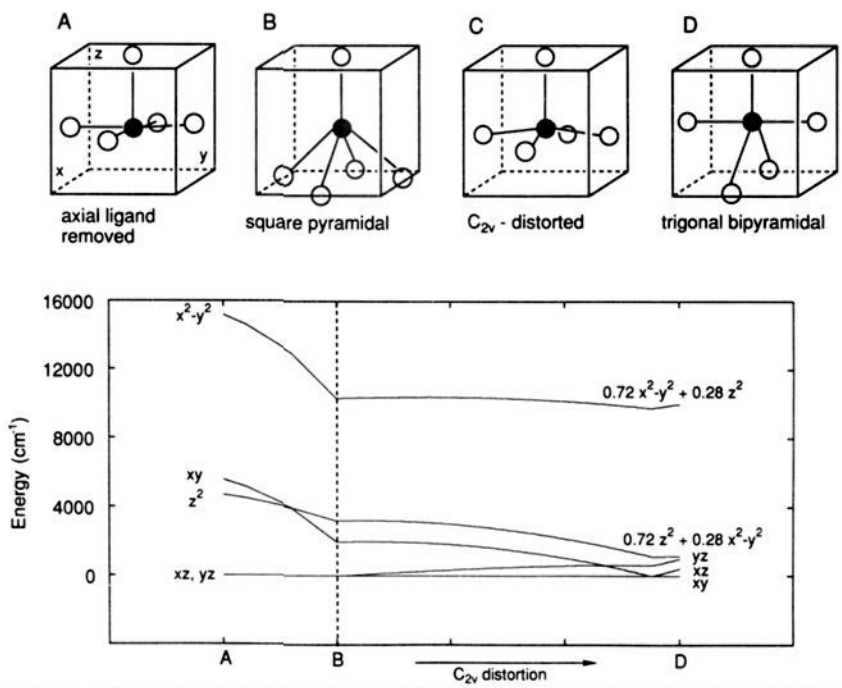

Figure 10. Relative d orbital energy levels connecting the square-pyramid (left) and the trigonal-bipyramid (right) along the Berry pseudorotation coordinate. The pseudorotation retains C_{2v} symmetry through the distortion. The discontinuity near the trigonal-bipyramidal limit results from a level crossing to produce a new ground state.

the metal 15° out of the ligand plane) and D_{3h} limits by maintaining a C_{2v} pathway.[67]

Since MMOH has primarily oxygen coordination, the calculations discussed below include four oxygen and one nitrogen ligand placed in the axial (or equatorial) position of the square-pyramidal complex. As indicated in Figure 10 a five-coordinate Fe^{2+} complex appears to have ligand field transitions $\leq$4000 cm^{-1} and one near-IR transition around 12 000 or 10 000 cm^{-1} for C_{4v} and D_{3h} structures, respectively, giving a Δ^5E_g of at least 7000 cm^{-1}. The Berry rotation involves a square-pyramidal geometry that has the central metal raised 15° out of the plane of the basal ligands. Decreasing or increasing this angle as the Fe^{2+} is moved toward or away from the ligand plane elongates or shortens the $Fe-L_{axial}$ bond. Lowering the $Fe-L_{axial}$ unit into the equatorial plane (structure A, left side of Figure 11) increases the ^5E_g splitting, since the ligand field repulsion is increased in the x,y plane raising the energies of the $d_{x^2-y^2}$ and d_{xy} orbitals. Alternatively, if the Fe^{2+} is raised more than 15° (structure B) out of the ligand plane with a reduced $Fe-L_{axial}$ bond length, the metal d_{z^2} orbital is destabilized since the shorter axial bond increases

(67) Note that the original C_{4v} coordinate system is used to describe the wave functions in the trigonal-bipyramidal case, such that the $d_{z'^2}$ orbital of a trigonal-bipyramidal site with z' being the C_3 axis is written as 75% $d_{x^2-y^2}$ + 25% d_{z^2} in the original coordinate system. With one nitrogen ligand D_{3h} symmetry is lost, and the coefficients deviate a few percent from the D_{3h} limit.

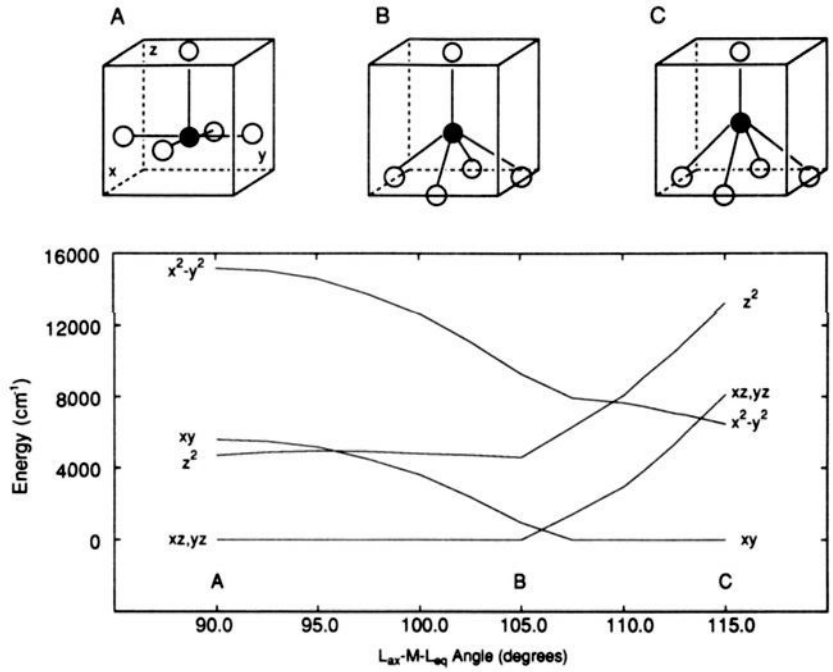

Figure 11. Ligand field energy level diagram calculated for a square-pyramidal Fe^{2+} site when the metal is moved away from the equatorial plane (L_{axial}–M–$L_{equatorial}$ = 90°) and the Fe–L_{axial} bond length is shortened.

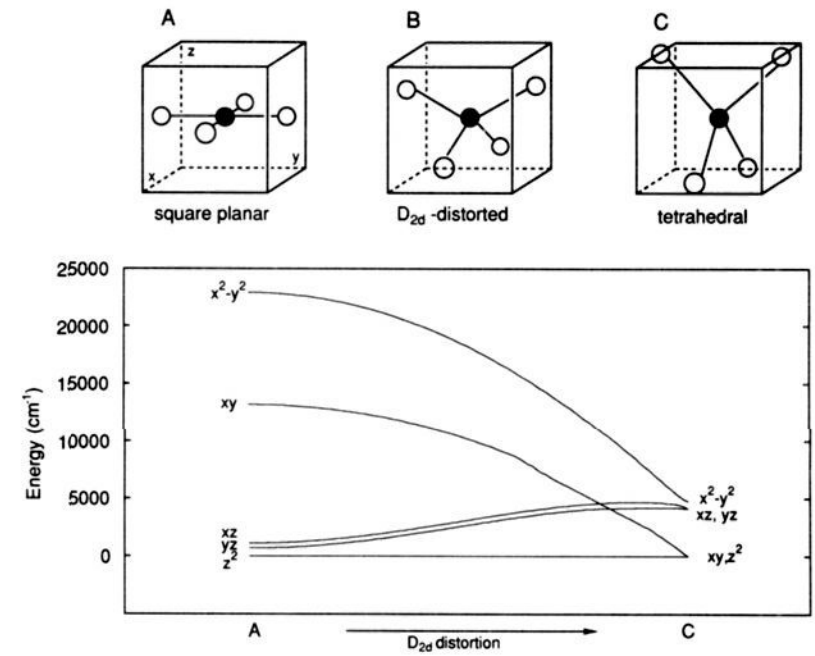

Figure 12. One electron d orbital energy level diagram for Fe(II) in a four-coordinate geometry. The ligands undergo a D_{2d} distortion as the molecule is distorted from square planar (left) into tetrahedral (right).

the repulsive interaction. In addition, as the metal is moved away from the equatorial plane the repulsion of the $L_{equatorial}$ set decreases lowering the energies of the $d_{x^2-y^2}$ and d_{xy} orbitals (middle of Figure 11) resulting in a reduced ^5E_g splitting. Finally, when the metal is moved further out of the equatorial plane (structure C), the repulsive interaction between the L_{axial} and metal d_{z^2} orbital dominates causing the z^2 and xz,yz levels to rapidly increase in energy (toward the right in Figure 11). As seen in Figure 11 (middle), a significant shift of the metal out of the equatorial plane can result in a smaller ^5E_g splitting ($\sim$4000 cm^{-1}) centered around the 7800 cm^{-1} region.

In the limit of large tetragonal elongation, one obtains a square-planar four-coordinate complex. Raising two *trans* ligands above and dropping the other *trans* ligand set below the equatorial plane results in a flattened tetrahedral structure (D_{2d}). Continued distortion of the ligands results in the formation of a tetrahedral complex (T_d), which has a doublet ^5E ground state and a triply degenerate $^5T_2$ excited state. Figure 12 presents a four-coordinate square-planar to tetrahedral correlation diagram for an Fe^{2+} complex with one nitrogen and three oxygen ligands.[68] Figure 12 illustrates that a square-planar Fe(II) complex is characterized by a ligand field transition at high energy ($\sim$20 000 cm^{-1}). As the complex distorts toward the tetrahedral limit the ligand field repulsion in the x,y plane is lowered and raised along z which greatly lowers the energy of the $d_{x^2-y^2}$ orbital until it becomes

(68) Note that the x and y axes for the D_{2d} and T_d geometries are rotated by 45° relative to the usual convention to allow a correlation of the $d_{x^2-y^2}$ HOMO over the geometries considered.

degenerate with the $d_{xz,yz}$ set in the T_d limit. The alternate axial distortion of a tetrahedral site is a C_{3v} elongation. The C_{3v} limit corresponds to that of a tetrahedron with one "axial" bond and the metal lowered toward the plane of the remaining three ligands. The axial bond length increases as the metal approaches the basal plane which causes the $^5T_2$ excited state of the tetrahedron to split into two components ($x^2 - y^2$ and xy, and z^2) separated by $\sim$4000 cm^{-1} at the C_{3v} limit.

These correlations between d → d spectra and geometry which have been developed through a combination of experiment and ligand field calculations provide a structural probe of the ferrous active sites of Hr and MMO. DeoxyN$_3$-Hr is known to have two six-coordinate ferrous atoms since the ligand field spectra show four transitions centered at 10 000 cm^{-1} (8500, 9600, 10 000, and 10 800 cm^{-1}).[30] This assignment is consistent with the ligand field calculations presented above. In the case of MMOH, on the other hand, only three transitions (7500, 9100, and 9900 cm^{-1}) are observed by CD and MCD (Figure 1) with at least one below the 8100 cm^{-1} limit for six-coordinate. These results lead to three possible spectral assignments: one six- and one four-coordinate Fe(II), one six- and one five-coordinate Fe(II), and two five-coordinate Fe(II). In the case of the six- plus five-coordinate Fe^{2+}s, an unresolved high energy transition should be present, while in the case of two five-coordinate ferrous ions an additional band at lower energy must be present.

In considering the possibility of six- plus four-coordinate Fe(II), a ligand field transition at 7500 cm^{-1} is possible toward the T_d limit (Figure 12, right). However, this flattened tetrahedron has the d_{z^2} orbital as the ground state which causes the axial zero-field splitting (D) to be greater than 0.[69] But from the spin Hamiltonian analysis of reduced MMOH presented earlier D must be less than 0 in order to have $J = 0.4 \pm 0.1$ cm^{-1}, $g_{\|} = 16$, and the (4,0;3,0) doublet as the first excited state at $\sim$5.0 cm^{-1}. Since the sign of D from geometrical considerations is not consistent with the spin Hamiltonian parameters, the possibility of a four-coordinate Fe(II) can be eliminated.

Both the sign and magnitude of D can be correlated to geometry. The axial ZFS splitting reflects the magnitude of the $^5T_2$ ground state splitting; the larger the splitting the smaller the value of D. D is expected to be -10 cm^{-1} or larger for a six-coordinate Fe(II) atom, while in the case of a five-coordinate complex the value of D would be expected to decrease.[70] The spin Hamiltonian parameters for deoxyN$_3$-Hr in Table II give values for D_1 and D_2 that lie between -13.0 and -15.0 cm^{-1}, while for MMOH D_1 ranged from -2.0 to -6.0 cm^{-1} and D_2 from -3.0 to -15.0 cm^{-1}. The decrease in D between deoxyN$_3$-Hr and reduced MMOH is therefore consistent with at least one Fe(II) becoming five-coordinate. However, the spin Hamiltonian fit to the data cannot distinguish between the possibility of two five-coordinate or one six- and one five-coordinate Fe(II) for MMOH.

The MCD and CD spectra of the reduced MMOH–component B complex show two low- and two high-energy bands (Figure 3). In addition, spin Hamiltonian analysis shows that both iron atoms have small negative D values which indicate that both Fe^{2+} are five-coordinate. Since the spin Hamiltonian parameters do not change dramatically between MMOH and the component B complex (Table II), the effects of component B on the reduced MMOH site can be regarded as a perturbation. Therefore, the active site of reduced MMOH is also likely to consist of two five-coordinate ferrous centers. The question of an unobserved ligand field transition in MMOH can be addressed by considering the fact that the lower limit on the axial ZFS for the component B complex is slightly higher than for MMOH. This suggests that the $^5T_2$ splitting has decreased, and thus the ^5E splitting of the excited state also decreases upon formation of the component B complex. This would be consistent with a low-energy band moving up in energy upon formation of the reduced component B complex.

The ligand field transitions observed can be interpreted in terms of the five-coordinate ligand field calculations presented in Figures 10 and 11 for a mixed ligand complex (one N and four O). It is apparent from Figure 10 that MMOH and the MMOH–component B complex do not have square-pyramidal or trigonal-bipyramidal limiting geometries since the d → d transitions observed at these extremes would be separated by more than $\geq$7000 cm^{-1}. However, in the square-pyramidal structure, the $d_{x^2-y^2}$ orbital is significantly stabilized as the Fe^{2+} center moves away from the equatorial ligand plane, while the metal d_{z^2} orbital is greatly destabilized due to increased repulsive interaction with the shorter Fe–L_{axial} bond. Figure 11 illustrates that as the $d_{x^2-y^2}$ and d_{z^2} orbital energies approach each other it is possible to have two ligand field transitions separated by approximately 2000 cm^{-1}, as is the case for the component B complex. Therefore, a distorted five-coordinate square-pyramidal structure is a reasonable description for each Fe^{2+} atom in the active site in the MMOH–component B complex.

Component B perturbs the MMOH MCD spectrum by apparently raising the energy of an unobserved band ($<$5000 cm^{-1}) to $\sim$6200 cm^{-1} and changing the sign of the 9800-cm^{-1} band from negative to positive. The 7700-cm^{-1} band remains unperturbed, and the shoulder seen in MMOH at $\sim$9000 cm^{-1} is unresolved in the MMOH–component B MCD spectrum but is observed at 8800 cm^{-1} in the CD spectrum. Thus it appears as if only one iron is significantly perturbed due to component B binding. The unperturbed Fe(II) in reduced MMOH exhibits two low-energy bands (7500, 9100 cm^{-1}) split by $\sim$2000 cm^{-1} which is consistent with a square-pyramidal geometry. The second Fe(II) of the reduced hydroxylase shows greater splitting between its ligand field bands ($>$4000 cm^{-1}) which could result from two possible geometric distortions: the Fe^{2+} could lie closer to the equatorial ligand plane in a square-pyramidal geometry or the Fe^{2+} could be in a more C_{2v} distorted environment. In either case, component B binding induces significant change in the geometry of this Fe(II) center.

Discussion

It is shown here that no perturbation in the CD spectrum is observed for (a) substrates that are readily turned over (e.g., *trans*-1,2-dichloroethylene), (b) products (e.g., methanol), (c) competitive substrate analog inhibitors (e.g., tetrachloroethylene), and (d) organic inhibitors known to bind within a few angstroms of the iron cluster from other spectroscopic studies (e.g., DMSO).[62] It is likely that each of these molecules bind in the MMOH substrate site, but the lack of a CD spectral perturbation strongly suggests direct binding to the iron is not involved. Direct binding would certainly require a change in the ligand field of the iron which would cause a readily detectable perturbation in the CD spectrum. This apparent failure of substrates and inhibitors to bind within bonding distance of the cluster iron suggests that mechanisms which invoke explicit formation of an iron–carbon bond as a reactive intermediate[71] at some point in the catalytic cycle are unlikely to apply to MMO. Rather, mechanisms in which substrates bind near the cluster as an iron-bound activated oxygen species is generated are compatible with both the data presented here and that presented in previous studies.[72]

In contrast to substrate and inhibitor binding results, the Fe(II)-Fe(II) active site is significantly perturbed when component B binds to MMOH. This is reflected primarily in the MCD spectrum of the MMOH–component B complex (Figure 3) by

(69) Varret, F.; Hartmann-Boutron, F. *Ann. Phys.* **1968**, *3*, 157–168.
(70) For high-spin Fe(II), since the splitting arises from coupling with the excited ligand field states,[54] which are at higher energy in lower symmetry, axial ZFS typically decreases as the complex symmetry decreases.
(71) Barton, D. H. R.; Csuhai, E.; Doller, D.; Ozbalik, N.; Balavoine, G. *Proc. Natl. Acad. Sci. U.S.A.* **1990**, *87*, 3401–3404.
(72) Priestley, N. D.; Floss, H. G.; Froland, W. A.; Lipscomb, J. D.; Williams, P. G.; Morimoto, H. *J. Am. Chem. Soc.* **1992**, *114*, 7561–7562.

the appearance of a new low-energy band and by the change in sign of the feature at ~9900 cm^{-1}. These MCD results suggest that the ligand field at one iron center of MMOH changes significantly upon binding component B to the reduced hydroxylase. Component B is a regulatory protein which increases the specific activity of the enzyme as much as 150-fold.[73] Since this increase in oxygen reactivity correlates with the change in ligand field environment of only one Fe(II) ion in the protein active site cluster, this Fe(II) ion perturbed by component B may play a dominant role in the oxygen reactivity.

DeoxyHr has one five-coordinate Fe(II) involved in O_2 binding while reduced MMOH and the MMOH–component B complex have two five-coordinate Fe(II) atoms in their active sites. The ligand field splitting of the ^5E_g excited state is obtained from the CD and MCD spectra and provides insight into the nature of the five-coordinate site. DeoxyHr has transitions at ~5000 and 10 000 cm^{-1},[30] MMOH at ~7500, 9100, and 9900 cm^{-1} and MMOH–component B at ~6200, 7700, 8800, and 9900 cm^{-1}. Therefore, deoxyHr has a ^5E_g splitting of ~5000 cm^{-1}, while MMOH has one Fe(II) with a splitting of ~2000 cm^{-1}, centered at ~7800 cm^{-1} (which is too low for six-coordinate), and another Fe^{2+} with $\Delta^5E_g > 4500$ cm^{-1}. For the component B complex the latter splitting decreases to ~3500 cm^{-1} while the former stays approximately the same. From the ligand field calculations in Figures 10 and 11, the decrease in splittings on going from deoxyHr to MMOH is consistent with an increase in the strength of the axial ligand interactions in a square-pyramidal structure.

Reduced MMOH is distinct from deoxyHr in that it is not inhibited by relatively high concentrations of several potential anionic ligands including NaN_3, KCN, NaCl, KF, and KOCN. Accordingly, we have shown here that even at relatively high concentrations no perturbation in the CD spectrum is observed for these molecules, suggesting that small anionic ligands do not bind to the iron. In the case of deoxyHr, anions such as azide appear to bind initially as HN_3,[30,74] and the proton they carry appears to be involved in protonating the OH^- bridge. As a direct consequence of this protonation, the coupling of the Hr cluster changes from antiferromagnetic to ferromagnetic indicative of the loss of the dominant super exchange pathway provided by the OH^-.[30] Our recent ENDOR and ESEEM results[57] show that the antiferromagnetic coupled cluster of half-met MMOH has an OH^- bridge. Thus, it is possible that by analogy with Hr, the ferromagnetism of fully reduced MMOH derives from protonation to form a H_2O bridge. EXAFS and ENDOR studies indicate that MMOH has more oxygen ligation than Hr.[39,62] This increased electron donor ligation would raise the pK_a of the bridging ligand relative to that in Hr leading to its further protonation to H_2O in reduced MMOH. The presence of a water bridge in fully reduced MMOH may also account for the low affinity of anionic ligands, because there would be no free base in the cluster to deprotonate these ligands as they associate. In the absence of such a base, ligands such as HN_3 would be poor ligands for a ferrous site.

These results for MMOH and the MMOH–component B complex have several possible mechanistic implications. It has been shown here that both iron atoms in the biferrous active site cluster are coordinatively unsaturated, that they are inequivalent, and that only one of these Fe(II) centers is significantly perturbed by component B. This suggests that molecular oxygen could bind in any of several *bidentate* orientations between these inequivalent iron centers resulting in the reduction of oxygen to a bridging peroxide. The inequivalent nature of the iron centers could polarize the oxygen–oxygen bond of the bridging peroxide resulting in the heterolytic cleavage and generation of an activated oxene species. Alternatively, the proposed water bridge of the reduced hydroxylase could serve as the active site source of two protons coupled to reduction of dioxygen (see Scheme I). That is, the reduction of dioxygen bound in a *monodentate* manner to one iron to the peroxy level would be facilitated by the protonation of the developing peroxide. Subsequent protonation of the terminal oxygen of the hydroperoxide would allow water to be the leaving group and thus assist in the heterolytic cleavage of the oxygen–oxygen bond resulting in the formation of an activated oxene species. Internal electron transfer between the iron atoms of the cluster would be greatly facilitated by the transient formation of an oxo bridge and therefore aid in the generation of an oxo-ferryl dimer intermediate.[8] A strongly antiferromagnetically coupled binuclear Fe(IV) species has, in fact, recently been observed in a freeze-quenched reaction of the reduced MMOH–component B complex with dioxygen.[75]

Scheme I

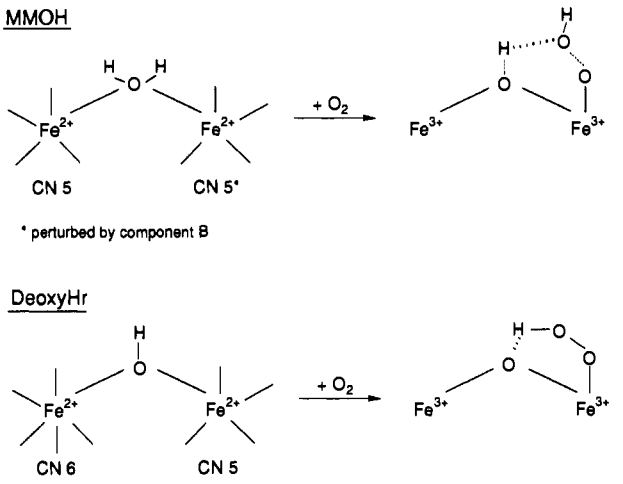

In the case of deoxyHr, only one iron center of the active site cluster has an open coordination position suggesting a *monodentate* binding mode for dioxygen (see Scheme I).[27] Furthermore, the hydroxo bridge in the deoxyHr active site cluster can only transfer one proton to the developing peroxide forming a stable, bent hydroperoxide complex.[76]

Reduced MMOH and deoxyHr both contain coupled binuclear iron clusters and yet have very different reactivities toward molecular oxygen. The spectroscopic protocol applied here has provided important insight into the active site structure of the binuclear iron clusters of these catalytically distinct proteins. Determination of the overall coordination geometries of each iron in the active site cluster and the nature of the bridging ligation between them for these proteins extends our understanding of the role of the protein ligand structure in effecting specific catalytic roles for this inorganic cofactor. Pulsed EPR studies on the reduced MMOH are currently underway[77] allowing us to further probe the nature of the bridging ligand responsible for the ferromagnetic coupling of the diferrous cluster. Application of the spectroscopic protocol presented above to probe substrate and small molecule interactions in the reduced MMOH–component B complex and the half-met form of this cluster are also presently underway.

Acknowledgment. This work was supported by the NSF-Biophysics Program Grant MCB 9019752 (E.I.S.) and a NIH Grant GM40466 (J.D.L.). We thank Dr. James McCormick for many useful interactions during the course of this study.

(73) Fox, B. G.; Liu, Y.; Dege, J. E.; Lipscomb, J. D. *J. Biol. Chem.* **1991**, *266*, 540–550.
(74) Bradic, Z.; Conrad, R.; Wilkins, R. G. *J. Biol. Chem.* **1977**, *252*, 6069–6075.
(75) Lee, S.-K.; Fox, B. G.; Froland, W. A.; Lipscomb, J. D.; Münck, E. *J. Am. Chem. Soc.* **1993**, *115*, 6450–6451.
(76) Shiemke, A. K.; Loehr, T. M.; Sanders-Loehr, J. *J. Am. Chem. Soc.* **1986**, *108*, 2437–2443.
(77) Thomann, H.; Bernardo, M.; Pulver, S.; Froland, W. A.; Lipscomb, J. D.; Solomon, E. I., unpublished results.